JADAVPUR UNIVERSITY

PG/AUE/S/121

IMPACT FORCE ANALYSIS OF FUNCTIONALLY GRADED MATERIAL PLATE USING FINITE ELEMENT METHOD

Submitted

By

SALAMAT MONDAL

Automobile Engineering

(Roll - 002011204002)

Guided

By

DR. TANMOY BANDYOPADHYAY

Department of Mechanical Engineering,

Jadavpur University

Kolkata – 700 032

Faculty of Engineering & Technology
Jadavpur University
Kolkata-700 032

We hereby recommend that the thesis, entitled as "force analysis of functionally graded material plate", prepared by Mr. SALAMAT MONDAL (Regn. No- 154335 of 2020-2021) under our guidance, be accepted in partial fulfillment of the requirement for the degree of Master of Technology (Automobile Engineer) from the Department of Mechanical Engineering of Jadavpur University.

.....

Adviser,
Dr. Tanmoy Bandyopadhyay
Department of Mechanical Engineering
Jadavpur University

Countersigned by:

.....	.....
Prof. Amit Karmakar	Prof. Chandan Mazumdar
Head,	Dean,
Department of Mechanical Engineering	Faculty of Engineering & Technology
Jadavpur University	Jadavpur University

Faculty of Engineering & Technology
Jadavpur University
Kolkata-700 032

Certificate of Approval

The foregoing thesis, entitled as "First Ply-Failure analysis of delaminated composite Plates" is hereby approved by the committee of final examination for evaluation of thesis as a creditable study of an engineering subject carried out and presented by Mr. Salamat Mondal (Regn. No- 154343 of 2020-2021) in a manner satisfactory to warrant it's acceptance as a perquisite to the degree of Master of Technology (Automobile Engineering). It is understood that by this approval, the undersigned do not necessarily endorse or approve any statement made, opinion expressed or conclusion drawn therein, but approve the thesis only for the purpose for which it is submitted. Committee of final examination for evaluation of thesis:

…… ……

…… ……

ACKNOWLEDGEMENT

It is a pleasant task to express my gratitude to all those who have assisted me in my project work.

First and foremost, I take this opportunity to express my sincere thanks and deepest sense of gratitude to my guide Dr Tanmoy Bandyopadhyay, Department of Mechanical Engineering, for their continuous, valuable guidance, suggestions and encouragement throughout the project work, which helped me a lot to improve this project work. Their appreciation during the good times has been boosting my morals and confidence.

I express my heartiest thanks to all the faculty members and research scholars of 'Automobile Engineering' laboratory, Department of Mechanical Engineering, Jadavpur University for their support and encouragement during the research work.

I am indebted to Prof. Amit Karmakar, Head, Department of Mechanical Engineering, Jadavpur University, for his kind help during this project work.

I am also grateful to all the faculty members of Mechanical Engineering Department for their moral support, immense help and co-operation during the course of this thesis work.

I would like to express my heart-felt gratitude to my parents, my relatives and my friends for their love and active support throughout the endeavor.

Date:
Salamat Mondal

ABSTRACT

The present work intends to estimate the low velocity impact response of FGM plates under the influence of critical parameters like power index, impactor velocity and the various FGM constituents. The finite element formulation is developed considering an eight-noded isoparametric plate bending element having five degrees of freedom at each node. The FGM plate is assumed to be cantilevered on one end to identify them as structural elements used in Turbomachinery and Fan blades. FGM are a special class of advanced materials where the material properties are assumed to be graded across the thickness of the FGM plate. These materials are therefore suited for applications wherein the material properties are needed to be different at different thicknesses of the plate. The mixture rule is employed to evaluate the material properties of the FGM plates for different power index values. The FGM material properties are assumed to vary smoothly across the plate thickness and the material properties at a certain thickness are evaluated. However most of the engineering components are subjected to random impact of moving foreign bodies during manufacture, transport and in field applications. The low-velocity impact phenomenon is detrimental to the life of the structural components made from FGM owing to their weak through-thickness strengths. In the present work, the FGM plate is assumed to be impacted centrally by a rigid spherical impactor moving normally at a certain initial velocity (VOI). The FGM plate is assumed to be oriented such that the metallic interface is at the bottom while the ceramic interface on the top of the plate. The impact is assumed to occur on the ceramic or the top side of the FGM plate and the contact between the ceramic surface and the steel ball is assumed to be frictionless and non-penetrative with the low impact velocities assumed to be 3m/s. In addition, the deformation of the spherical impactor is assumed to be negligible and any heat dissipation due to the impact phenomenon is neglected. The Lagrangian principle is assumed to arrive at the equations of motion of both the FGM plate and the spherical impactor. The deflections in the FGM plate are derived based on the First-order shear deformation theory while the assembled mass and the stiffness matrices of the FGM plate are arrived at based on the Finite Element Methods. The dynamic equilibrium equations are then solved to extract the transient response of FGM plate at suitable time steps based on the Newmark's Time integration scheme. The contact force, plate and impactor displacements and the impactor velocities are plotted again the elapsed time and analyzed in the present work. The effects of some critical defining parameters like power index, impactor velocity and FGM combinations on the transient response of FGM plate are the outcomes of the present analysis.

TABLE OF CONTENTS

NOMENCLATURE

1, 2, 3	Coordinate system of lamina in principal material direction.
A	Area of the plate
A_e	Area of the element
A_{ij}	Extensional stiffness coefficients of the laminate, where(i, j = 1, 2, 4, 5,6)
a, b	Sides of the plate along x and y axes, respectively
[B]	Strain-displacement matrix
[Bij]	Coupling stiffness of the laminate, where (i, j = 1, 2, 6)
C/L	Normalized crack length
[D]	Elasticity matrics
[Dij]	Bending stiffness of the laminate (i, j = 1, 2, 6)
E	Young's Modulus of plate
E1, E2	Young's Modulii of the lamina along 1 and 2 axes respectively
FEM	Finite element method
G12,G13,G23	Shear Moduli of a lamina in 1-2, 1-3, 2-3 planes respectively
h	Thickness of the laminate
hr	Relative position of de-lamination
[J]	Jacobian matrix
$[k_e]$	Element stiffness matrix
k_x, k_y, k_{xy}	Curvature
M_x,M_y,M_{xy}	Moment resultants
Nx,Ny,Nxy	Internal force resultants
Ni	Shape function
n	Number of lamina in the laminate
Q_x, Q_y	Transverse shear resultant
$[Q_{ij}]$	Matrix of stiffness coefficient
$[\bar{Q}_{ij}]$	Matrix of reduced stiffness coefficients
R_x ,R_y	Radius of curvature
R_{xy}	Radius of twist
U	Total potential energy
u, v, w	Displacement in x, y, z direction respectively
u^0, v^0, w^0	Displacements of the mid-surface in x, y and z directions respectively
u_i,v_i,w_i	Displacements at node i
X_i,Y_i	Nodal x and y coordinate
X,Y,Z	Cartesian coordinate system
Z_k,Z_{k-1}	Top and bottom distance of a kth lamina from the mid-surface
α	Shear Correction Factor
$\gamma_{xy}, \gamma_{xz}, \gamma_{yz}$	Shear strains in x-y, x-z and y-z planes respectively
γ_{xy}^0	Shear strain of mid-surface in x-y plane
$\varepsilon_1, \varepsilon_2$	Strains of a laminae along the principal axes respectivelyξ , η
$\varepsilon_x, \varepsilon_y$	Strains along x and y axes respectively
$\varepsilon_x^0, \varepsilon_y^0$	Strains of the mid-surface along x and y axes respectively
ξ, η	Local natural coordinates axes of the element
ξ_i, η_i	Nodal values at i
$\gamma_{12}, \gamma_{13}, \gamma_{23}$	Shear strain in 1-2, 1-3 and 2-3 planes respectively
θ	Fibre orientation about x-axis
θ_x, θ_y	Rotations of the plate about x and y axes respectively

θ_{xi}, θ_{yi}	Nodal values of θ_x and θ_y respectively
ν	Poission's ratio of the laminate
ν_{12}, ν_{21}	Poission's ratio of laminate in 1-2 and 2-1 planes respectively
σ_1, σ_2	Normal stresses in a lamina along 1 and 2 axes respectively
σ_x, σ_y	Normal stresses along x and y axes respectively
$\tau_{12}\tau_{13}\tau_{23}$	Shear stresses in a lamina in 1-2, 1-3 and 2-3 planes respectively
Ω	Non-dimensional frequency parameter
ω_0	Natural frequency
ρ_k	Density of a k^{th} lamina
bo	Reference width of thin shallow conical shell
θ_v	Vertex angle of cone
θ_0	Base subtended angle of cone
ψ	Angle of twist

Subscript
k Number of the lamina
Superscript
T Transpose of a matrix

Chapter-1

INTRODUCTION

Because of their inherent mechanical properties, such as high strength, modulus of elasticity, and decreased specific gravity, FGM materials are widely used. It is now possible to design new FGM materials with superior physical and mechanical qualities as a consequence of extensive research into metallurgical features of materials and a better understanding of structural properties. This is feasible because of the FGM's material composition, which changes in a favored direction according to a specified regulation. FGM's (functionally graded materials) are one of the most advanced materials that can endure high temperatures. FGMs are made up of a constantly changing mix of two distinct materials. One is an engineered ceramic that can withstand the high-temperature environment's thermal loading, and the other is a light metal that can preserve structural stiffness. The class of materials known as composites, in which one type of hybrid material is functionally graded materials, has already achieved great performance achievements (FGMs). Functionally graded material (FGM) is an example of a material whose properties may be used to meet specific requirements in a variety of engineering applications. Almost every aspect of everyday life, from the bicycle to the automobile, was revolutionized in the latter half of the twentieth century. The FGM's are a new class of materials that have a significant impact on everything from spacecraft to apparel to construction. High-performance materials, such as FGM's, have also enabled some of the century's most remarkable technological breakthroughs in biomedical, optoelectronics, spaceflight, chemical, mechanical, and other engineering fields.

1.1.1 *PREAMBLE*

With the advancement of modern technology composite materials have become an important class of materials due to their wide range of applications. Composites are highly advantageous because of their light weight, strength, design flexibility, and corrosion as well as wear resistance. The disadvantage of composites is they fail by delamination due to sharp transition of properties at the junction. To overcome this an advanced type of composite material named functionally graded materials (FGMs) was first proposed by the Japanese researchers for an aerospace project in 1984 **[1]**. The usefulness of functionally graded composites with a graded structure concept was previously recognized by **Shen and Bever** in 1972 **[2].**

FGMs are novel kinds of advanced composites which are primarily composed of metals at one surface and ceramics at the other. This is achieved by gradually varying the volume fraction of the constituent materials along the thickness. Thus, there is smooth transition of the material properties like Young's Modulus, Poisson's ratio, Shear Modulus, density, and coefficient of thermal expansion which relaxes the stress concentrations and delamination generally observed

in layered structures. The metal part provides excellent strength and toughness, whereas the ceramic part imparts the ability to withstand high temperature environment. Therefore, FGMs have attracted the attention of a lot of researchers in the past few decades due to their potential application in spacecrafts, nuclear power plants, automobile industries, biomedical equipment and other weight-sensitive applications.

Since this area is relatively new, industrial application and published literature on the behaviour of FGM plates is limited. In general, FGM can be used in underwater vehicles, spacecrafts, leading edge of an aircraft wing, automobile bodies/protruded sections, blade of steam turbines and jet engines etc where the structures may experience variable environment. Turbo-machinery blades with low aspect ratio can be idealized as cantilever plates made of functionally graded material.So it is important to study the vibrational behaviour of the structure to ensure safety and reliability in operation. In present study, the free vibration characteristics of FGM cantilevered flat plate for different volume fractions, aspect ratio, porosity type and twist angle are demonstrated and discussed. To achieve this an eight-nodedisoparametric shell element is developed for the present finite element formulation. The power law is employed to evaluate the material properties of FGM plate at different points.

1.1.2 *TURBOMACHINERY BLADES*

The development of high-speed turbomachineries (i.e. turbines, compressors, fans and blowers) in the early 1950s resulted in the search for advanced materials that could resist the high temperature and the associated dynamic stress generated on the turbomachinery components. The failure of the turbine or turbo-compressor blades especially due to fatigue became a critical issue for researchers. The failure of the turbine blades was especially found to occur while vibrating near their resonant frequencies. As such, the accurate prediction of the natural frequencies of the turbomachinery blades became a topic of considerable research interest during the design phase itself. Owing to the fact that there are numerous fixed and rotating blades in a turbo-machine the accurate point of failure of such a system is extremely complex and hence requires very careful design. The advent of the FGM materials with their superior heat-resistant properties combined with their excellent strength has proven to be a boon for applications as turbine and fan blades in industrial applications.

1.1.3 *DYNAMIC BEHAVIOUR*

Blades are the vital part of a turbomachine since they are subjected to extreme dynamic loading during operation owing to rotation and random vibrations. The performance characteristics of these machines are largely dependent on the shape and geometry of the blades and hence their dynamic behavior is of considerable importance as far as the reliability and life of an engine is concerned. The major causes of failure of blades are fatigue in the lower temperature stages of a turbine or an axial flow compressor. In high temperature applications as in thermal power plants,

the property degradation of composite blades leads to a reduction in their strength and stiffness thereby leading to failure at much reduced loads. Blade failure due to fatigue is predominantly the consequence of resonant vibrations which gets aggravated at high temperatures. Such failures may be quite costly both in terms of safety and maintenance of turbine engines.

Although a turbine is designed to avoid resonance at its steady operating speed, it experiences resonance several times during the starting up and shutting down of the turbine. This may lead to shutdown because of blade failure. In general, it is found that nearly all the vibrations of the blades are closely related to their natural frequencies. Thus an in-depth knowledge of these frequencies is of fundamental importance to the designers in order to prevent vibration induced failures and ensure long life structurally sound blades.
However, an accurate prediction of these natural frequencies is usually very difficult because of the uncertainty of the excitation. It is equally difficult to predict the contribution of the complex blade geometries as well as the harmful effects of elevated temperature on such structures. The classic design practice for such blades has been mainly to rely on the blade natural frequencies to avoid harmful blade resonances. The natural frequencies are found by modeling the blades as cantilever plates and taking into account all the geometric complexities involved. The frequencies are determined at both stationary and rotating conditions taking into account the initial stresses resulting from rotation.

1.1.4 *FINITE ELEMENT METHOD*

The solution to the elasticity problems in the static and dynamic response of civil and aeronautical structures became much simplified with the introduction of high speed computers in 1950s and 1960s. Finite element method (FEM) is a numerical technique to find approximate solutions of boundary value problems involving partial differential equations. This involves 4 discretization of the domain into various smaller sub-domains, known as finite elements, generating element equations for each of the finite elements, assembling the element equations of all the elements at specified nodes to generate the global equations which are then solved using appropriate solution techniques. The vibration of the composite shells involves many complex interactions between the shell structure, laminate properties, delamination behavior, internal strains, initial stresses and impact of foreign bodies. The solution of such problems is highly complex, computationally intensive and involves very large matrices. The availability of the modern high speedcomputers and finite element software code NASTRAN along with the commercial software packages like ANSYS, ALGOR, COSMOS/M and ABACUS have been helpful in obtaining solution of problems in static and dynamic structural analysis, fluid flow, thermal analysis, electromagnetic and seismic response. The choice of a proper mathematical model, optimal discretization criteria and an appropriate solution technique is the prime requisite of any finite element simulation since it determines the closeness, reliability and its usability for modeling complex engineering applications.

1.1.5 *LIMITATIONS OF FEM*

The finite element method is an approximate technique and the accuracy of the simulation results are largely dependent on the choice of the finite elements used in the discretization process. The solution to the differential equations are obtained only at the nodal points and sometimes may not be representative of the response of an entire domain in case of complex geometries, irregularities in shape, curvature, unsymmetric stress distribution or non-linear behaviour. Thus it becomes extremely essential to ascertain that the finite element modelling conforms to each and every aspect of a complex problem. The accuracy of the FEM method must also be thoroughly validated against experimental results incorporating numerous cycles of mesh enhancement/ refinement and error analysis until a required degree of precision is arrived at in what is known as an adaptive finite element analysis. In addition most finite element simulations are computation intensive and may require large computation time and resources which must also be optimized for better design cycle time and cost reduction.

LITERATURE REVIEW

FGMs have been intensively examined by researchers since the notion was initially presented, with a focus on their thermo-elastic characteristics. Noda [1] provided a comprehensive discussion of thermal stress in FGMs subjected to a steady-temperature field or thermal shock. The material gradation in finite element method can be achieved by various ways. The simplest method to do so is dividing the FG plate into various isotropic layers. This method leads to sudden jump in material properties at the interface of each layers that leads to the development of stress concentration region. To achieve accuracy through this method, one need to divide the geometry into many isotropic layers [2]. Most appropriate method can be discretizing the domain with a specially formulated element with embedded material gradation along certain direction, which requires considerable amount of programming skill [3]. The pseudo temperature method to implement the material gradation [4] can serve the purpose well, which not only takes care of smooth variation of material properties but also is easier to implement. This is a unique method as this completely avoids the layers wise modeling thereby saving time and computational power, one of the main benefits of such modeling is that it does not require high end mathematics for modeling and gives almost exact result [5]. Singh and Harsha [6] investigated the nonlinear dynamic analysis of a sandwich SFGM plate lying on a Pasternak foundation under thermal environment. Grover et al. [7] Using a new non-polynomial shear-deformation theory, researchers investigated the structural behavior of laminated composite and sandwich plates. Gupta et al. [8] investigated the vibration characteristics of geometrically non-uniform functionally graded plates with mixed boundary conditions Merdaci et al. [9] used HSDT based on the Navier-type approach to investigate the free vibration response of FG plates with varying porosity distributions in the thickness direction. To increase the load-carrying capacity of thin-walled structures while

maintaining their lightweight nature, it is purposeful not to increase their thickness but, on one hand, to apply modern composite, hybrid or special materials, e.g., Functionally Graded Materials (FGM) [10], or to use all types of stiffeners [11]. An application of stiffeners requires, however, a more detailed analysis, including a phenomenon of interactive buckling, which affects considerably the load-carrying capacity of thin-walled structures under compression in the elastic range. Reddy and Cheng [12] and Wang et al. [13] predicted thermo-elastic responses in FGM plates using asymptotic methods. Yihunieet al. [14] discussed the effect of volume fraction index on thermal properties like conductivity and expansion coefficient in radial directions in a thick walled FGM cylinders. It was observed that the temperature distribution is not homogeneous. Anthony Xavior et al., [15] manufactured a synthesized FGM by varying its densities along width using additive manufacturing technology. Kiani et al. (16) studied the Low velocity impact response of an FGM beam with through-the-thickness distributed properties. jam and Kiani (17) analysed the response of functionally graded carbon nanotube reinforced composite (FG-CNTRC) beam subjected to the action of an impacting mass. Mirzaei and Kinai (18) investigated the free vibration characteristics of composite plates reinforced with single walled carbon nanotubes. Mao et al. (19) developed a modified contact model to deal with impact problem of the functionally graded shallow spherical shell in thermal environment. Eghtesad, and Shafiei [20] studied in Problems with large deformation including fracture and fragmentation, the grid based methods have some limitations which make them unsuitable for simulating these types of problems. In the study of the vibration characteristics of composite plates and shells among which the most notable work was carried out by Qatu and Leissa [21] to determine the natural frequencies of stationary composite plates. Liew et al. [22] investigated the vibration characteristics of pretwisted cantilever shallow conical shells by using Ritz method. McGee and Chu [23] carried out three-dimensional continuum vibration analysis of rotating, laminated composite blades using the Ritz method. The work by Lee et al. [24] focused on the vibrationof twisted conical composite shells using finite element method.The behavior of delaminated composite beams and plates has been fairly established in the works of Shen and Grady [25], Krawczuket al. [26], Tracy and Pardoen [27], Paolozzi and Peroni [28] and Teneket al. [29]. Karmakar and Kishimoto [30] extended this analysis for delaminated composite pretwisted rotating shells based on finite element method. Whitney and Ashton [31], Dhanarajand Palani-nathan [32] and Sai Ram and Sinha [33] studied the effects of temperature and moisture concentration on the free vibration response of laminated composite plates. This was extended in the study of multiple delaminated composite plates and shells in hygrothermal environment by Parhi et al. [34]. In addition, the hygrothermal effects on the bending characteristics [35] and the buckling [36] of laminated composite plates have also been analyzed. Naidu and Sinha [37] studied the non-linear vibration of laminated composite shells in hygrothermal environment incorporating the Green–Lagrange strains. The pioneering works in the field of the impact response of composite plates have been carried out by Sun and Chattopadhyay [38] and Sun and Chen [39] using analytical and finite element methods respectively. Chun and Lam [40] presented a numerical method using Lagrange's principle and

Hertzian contact law in calculating the dynamic response of laminated composite plates under low-velocity impact of a mass. Sekine et al. [41] and Hu et al. [42] presented the impact response of composite laminates containing delamination when impacted by a rigid ball using finite element methods.

Later work by Karmakar and Kishimoto [43] focused on the thermodynamic behavior of composite shells subjected to single-site impact. However in most practical applications as in hailstorm or ballistic attacks, impact on composite laminates is never a localized phenomenon and the loading and unloading cycles of multiple impactors can greatly influence the contact force and displacement. The residual strength of composite laminates with multiple impact damage has been studied experimentally by Jones [44].Lam and Sathiya moorthy [45] analyzed the low velocity impact response of a system consisting of a laminated beam and multiples spherical impactors using a higher-order shear deformation theory. Chakraborty [46] presented a 3D finite element analysis for assessing the impact response and delamination induced at the interfaces in graphite-epoxy laminated plates subjected to low velocity impact of multiple cylindrical impactors. Ghosh[47] analyzed the hygrothermal effects on the initiation and propagation of damage in composite shells due to low-velocity impacts giving insight into the effects of environment in impact problems.

In recent years, Reid et al. [48] studied the Low Velocity Impact Analysis of Functionally Graded Circular Plates. Shariyat and Farzan **[49, 50]** investigated the response of an FGM plate in rectangular shape and graded circular plate under the eccentric impact. In that research, the first order shear deformation beam theory was used and the effect of in-plane loads was also taken into consideration. Khalili et al. **[51]** studied the response of a thin FGM plate in rectangular shape that was subjected to low velocity impact. In another study, Dai et al. **[52]** studied the low velocity impact behaviour of shear deformable FGM circular plates. The solution in space and time domains was obtained based on the orthogonal collocation point method and Newmark's method, respectively.

PROCESSING TECHNIQUES OF FUNCTIONALLY GRADED MATERIALS(FGM) :

Surface coatings are the most common type of thin functionally graded materials. Depending on the service demand from the process, there are a variety of surface deposition procedures to choose from.

a) Vapour Deposition Technique:

Sputter deposition, Chemical Vapour Deposition (CVD), and Physical Vapour Deposition are all examples of vapour deposition processes (PVD). These methods of vapour deposition are used to

manufacture functionally graded surface coatings with excellent microstructure, although they can only be utilised to deposit thin surface coatings. They consume a lot of energy and emit hazardous fumes as a consequence. Plasma spraying, to make functionally graded coatings, electro deposition and other processes are used. Ion Beam Assisted Deposition (IBAD), Self-Propagating High-Temperature Synthesis (SHS), electro phoretic, etc. All of the aforementioned procedures are uneconomical to utilize in the production of bulk FGM since they are slow and energy demanding. The following are some of the fabrication methods for generating bulk functionally graded materials.

b) Powder Metallurgy (PM):

Powder metallurgy (PM) is a process that uses three main steps to generate functionally graded material: weighing and mixing powder according to a pre-designed spatial distribution determined by the functional requirement, stacking and ramming premixed powders, and finally sintering. The PM approach produces a progressive structure. The centrifugal approach is utilized when a continuous structure is sought.

c) Centrifugal Method:

The centrifugal process is comparable to centrifugal casting, in which the force of gravity is utilized to make bulk functionally graded material by rotating the mould. Because of the difference in material densities and the spinning of the mould, graded material is created in this manner. There are other similar techniques in the literature, such as the centrifugal method (e.g. gravity method, etc.). Even though continuous grading is possible, only cylindrical objects can be created using the centrifugal process. Another issue with the centrifugal approach is that the types of gradients that can be produced are limited because the gradient is formed by natural processes (centrifugal force and density difference). Researchers are adopting an alternate manufacturing approach known as solid free from to tackle these issues.

MATERIAL GRADIENT OF FGM PLATE

The material properties in the thickness direction of the FGM plates vary with power law functions. A mixture of the two materials composes the through-thickness characteristics. The FGM plate is modeled usually with one side of the material being ceramic and the other side being metal.

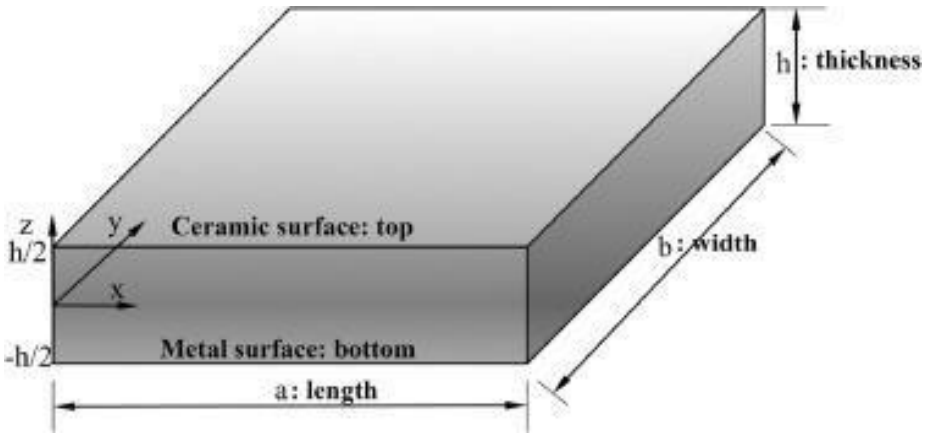

Fig.1 Details of a FGM plate

The graded material properties of the FGM plate at a certain thickness, *z*, measured from the mid-plane of the FGM plate is denoted by

$$P(\mathrm{z}) = (P_{\mathrm{c}} - P_{\mathrm{m}})\mathrm{V_c} + P_{\mathrm{m}} \tag{1}$$

The graded material properties of a FGM plate is assumed to be based on the power law that assumes a smooth transition of the material properties from metallic interface at the bottom to the ceramic interface at the top surface of the FGM plate expressed as

$$E(z) = \left\{(E_C - E_M) * \left[0.50 + \left(\frac{z}{h}\right)\right]^k + E_M\right\} \tag{1a}$$

$$\rho(z) = \left\{(\rho_C - \rho_M) * \left[0.50 + \left(\frac{z}{h}\right)\right]^k + \rho_M\right\} \tag{1b}$$

$$\nu(z) = \left\{(\nu_C - \nu_M) * \left[0.50 + \left(\frac{z}{h}\right)\right]^k + \nu_M\right\} \tag{1c}$$

$$\alpha(z) = \left\{(\alpha_C - \alpha_M) * \left[0.50 + \left(\frac{z}{h}\right)\right]^k + \alpha_M\right\} \tag{1d}$$

where, P_{c} and P_{m} denote the properties of the ceramic and metallic interfaces, respectively.

$$V_c = \left(\frac{z}{h} + \frac{1}{2}\right)^k, \qquad k \geq 0 \tag{2}$$

where *k* is the FGM Power factor, *h* is the thickness of the plate, V_{c} is the volume fraction of the ceramic part and *P* represents the effective material property of the FGM plate.

FINITE ELEMENT FORMULATION

2.2 *GOVERNING EQUATIONS FOR A LAMINAR STRUCTURE*

The FGM structure may be assumed to be consisting of different layers rigidly bonded together such that each layer has its material properties as a intermediate between the metal and ceramic constituent present at the bottom and top layers respectively. Each such lamina may be assumed to be isotropic with the properties being calculated at the mid-plane of the layer. The number of such lamina comprising the FGM may be obtained by performing convergence studies which such that the layered analysis may yield accurate results regarding the free vibration behavior of the FGM structure as a whole. The present analysis is carried out considering the FGM plate to be comprising of ten such constituting layers based on convergence studies. The basic behavior of a unidirectional lamina as shown in Fig 2.3 is assumed to be linearly elastic. The most common form of expressing the stress- strain relations of an orthotropic lamina involves plane stress conditions and engineering constants.

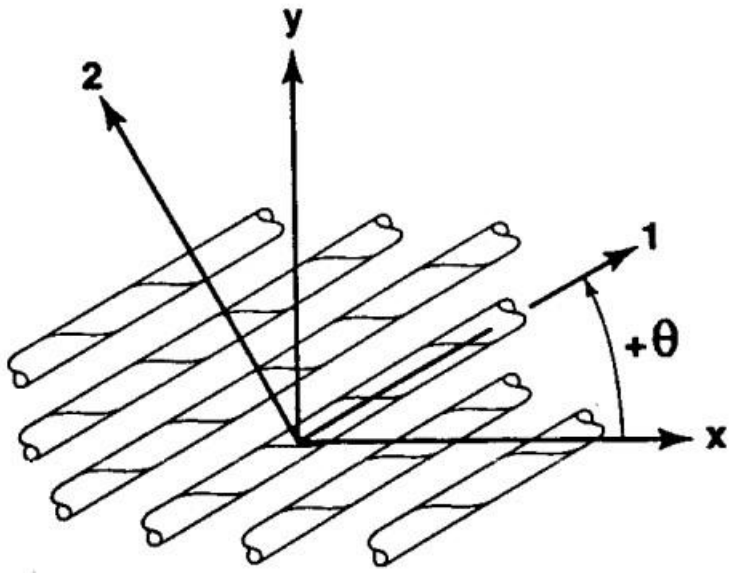

Fig. 2 An arbitrary oriented laminate
(Positive rotation of principal material axes from x-y axes[57])

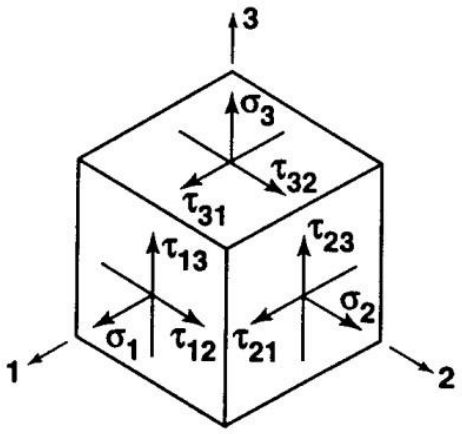

Fig 3. Stresses on an element

Neglecting the normal stress perpendicular to the plate of the lamina, the stress-strain relations, in the principal material direction 1, 2 and 3 (Fig 2.2) are given by

$$\begin{bmatrix} \sigma_1 \\ \sigma_2 \\ \tau_{12} \end{bmatrix} = \begin{bmatrix} Q_{11} & Q_{12} & 0 \\ Q_{12} & Q_{22} & 0 \\ 0 & 0 & Q_{66} \end{bmatrix} \begin{bmatrix} \varepsilon_1 \\ \varepsilon_2 \\ \varepsilon_3 \end{bmatrix}$$

(2.3a)

$$\begin{bmatrix} \tau_{13} \\ \tau_{23} \end{bmatrix} = \begin{bmatrix} Q_{44} & 0 \\ 0 & Q_{55} \end{bmatrix} \begin{bmatrix} \gamma_{13} \\ \gamma_{23} \end{bmatrix}$$

(2.3b)

Where,

$$Q_{11} = E_1 / (1-\nu_{12}\nu_{21})$$

$$Q_{12} = \nu_{12}E_2/ (1- \nu_{12}\nu_{21})$$

$$Q_{22} = E_2/ (1- \nu_{12}\nu_{21}) \qquad (2.4)$$

$$Q_{66}=G_{12},\ Q_{44}=G_{13},\ Q_{55}=G_{23}$$

The stress-strain relations of the lamina, with respect to the x, y and z axes (Fig 2.3), are expressed as

$$\begin{bmatrix} \sigma_x \\ \sigma_y \\ \sigma_{xy} \end{bmatrix} = \begin{bmatrix} \bar{Q} \end{bmatrix} \begin{bmatrix} \varepsilon_x \\ \varepsilon_y \\ \varepsilon_{xy} \end{bmatrix} = \begin{bmatrix} \bar{Q}_{11} & \bar{Q}_{12} & \bar{Q}_{16} \\ \bar{Q}_{12} & \bar{Q}_{22} & \bar{Q}_{26} \\ \bar{Q}_{16} & \bar{Q}_{26} & \bar{Q}_{66} \end{bmatrix} \begin{bmatrix} \varepsilon_x \\ \varepsilon_y \\ \varepsilon_{xy} \end{bmatrix}$$

(2.5a)

$$\begin{bmatrix} \tau_{xz} \\ \tau_{yz} \end{bmatrix} = \begin{bmatrix} \bar{Q}_{44} & \bar{Q}_{45} \\ \bar{Q}_{45} & \bar{Q}_{55} \end{bmatrix} \begin{bmatrix} \gamma_{xz} \\ \gamma_{yz} \end{bmatrix}$$

(2.5b)

Where

$$\overline{Q_{11}} = Q_{11}\text{Cos}^4\theta + 2(Q_{12} + 2Q_{66})\text{Sin}^2\theta\,\text{Cos}^2\theta + Q_{22}\text{Sin}^4\theta,$$

$$\overline{Q_{12}} = (Q_{11}Q_{22} - 4Q_{66})\text{Sin}^2\theta\text{Cos}^2\theta + Q_{12}(\text{Sin}^4\theta + \text{Cos}^4\theta),$$

$$\overline{Q_{22}} = Q_{11}\text{Sin}^4\theta + 2(Q_{12} + 2Q_{66})\,\text{Sin}^2\theta\text{Cos}^2\theta + Q_{22}\text{Cos}^4\theta,$$

$$\overline{Q_{16}} = (Q_{11} - Q_{12} - 2Q_{66})\text{Sin}\theta\text{Cos}^3\theta + (Q_{12} - Q_{22} + 2Q_{66})\text{Sin}^3\theta\text{Cos}\theta$$

$$\overline{Q_{26}} = (Q_{11} - Q_{12} - 2Q_{66})\text{Sin}^3\theta\text{Cos}\theta + (Q_{12} - Q_{22} + 2Q_{66})\text{Sin}\theta\text{Cos}^3\theta$$

$$\overline{Q_{66}} = (Q_{11} + Q_{22} - 2Q_{12} - 2Q_{66})\text{Sin}^2\theta\text{Cos}^2\theta + Q_{66}(\text{Sin}^4\theta + \text{COs}^4\theta)$$

$$\overline{Q_{44}} = Q_{44}\text{Cos}^2\theta + Q_{55}\text{Sin}^2\theta$$

$$\overline{Q_{45}} = (Q_{55} - Q_{44})\text{Sin}\theta\text{Cos}\theta$$

$$\overline{Q_{55}} = Q_{55}\text{Cos}^2\theta + Q_{44}\text{Sin}^2\theta$$

(2.6)

2.3 *FINITE ELEMENT STRUCTURAL ANALYSIS*

A laminated plate (Fig. 2.5) can be regarded as consisting of unidirectional laminate bonded together to act as an integral part. The bonds are infinitesimally thin and are non-shear deformable. Hence, the displacements are continuous throughout the thickness of the laminate. The following assumptions are made according to the Yang-Norris-Stavasky theory **[58]** which is a generalization of the Mindlin's theory to laminated plates.

- The deflection of the laminated plate is small.
- Normal to the mid surface before deformation remains straight but is not necessarily after deformation.

- Stresses normal to the mid surface are neglected.

The analysis is made by considering a laminated plate as considered in Fig. 2.5. The layer details of the laminate are shown in Fig. 2.6.

The in-plane displacements of a plate *u* and *v* of any point at a distance z from the mid-surface are given by

$$u\,(x, y, z, t) = u^0\,(x, y, t) + z\theta_y(x, y, t)$$
$$v\,(x, y, z, t) = v^0\,(x, y, t) - z\theta_x(x, y, t)$$
$$w\,(x, y, z, t) = w^0(x, y, t) \qquad (2.7)$$

Where, *u*, *v* and *w*are displacements in *x*, *y* and *z* directions, respectively, and the superscript (^{0}) corresponds to the mid-plane values. Here, θ_x and θ_y denote the rotations of the cross-sections perpendicular to the *x*- and y-axis respectively.

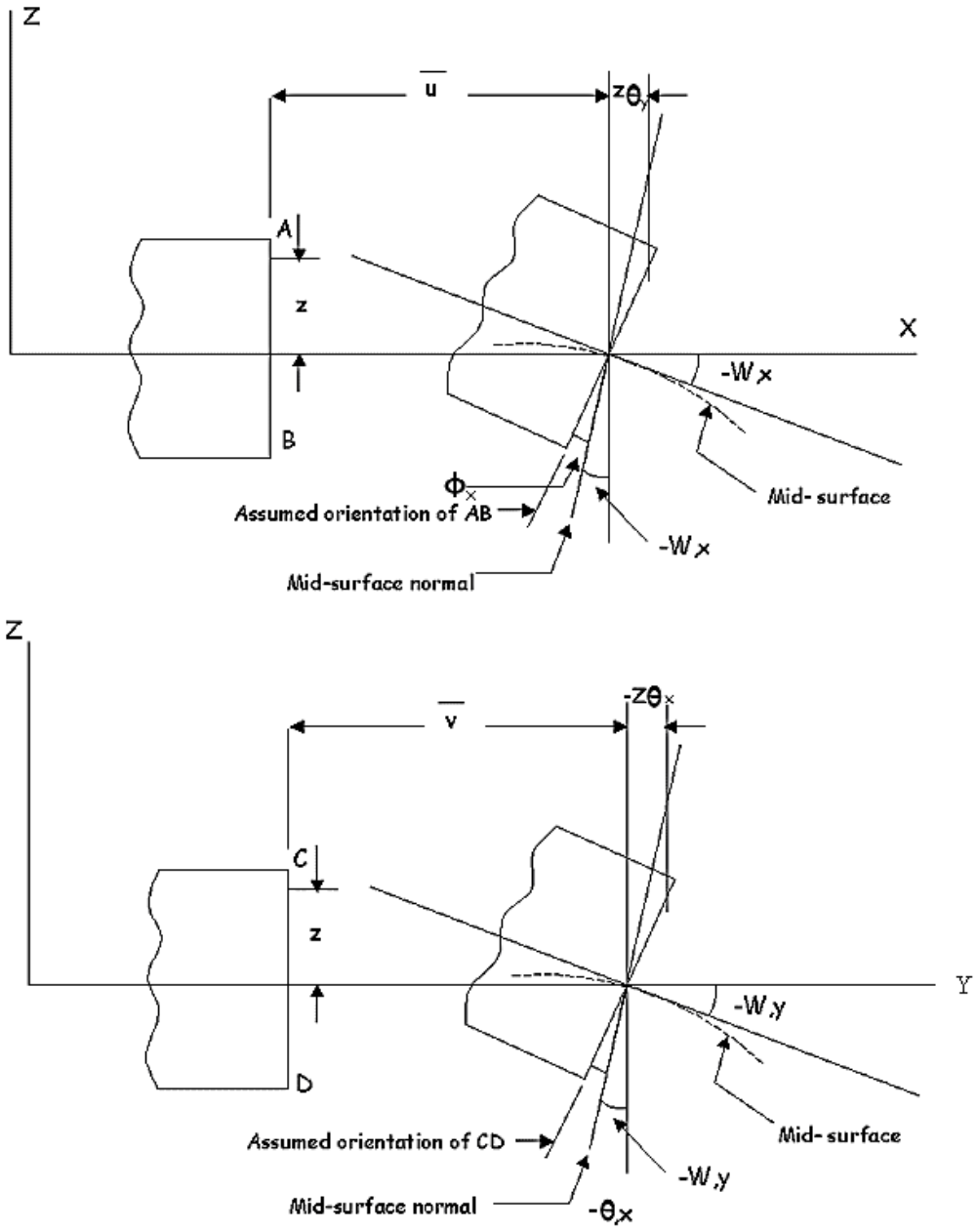

Fig. 4 Plate deformation

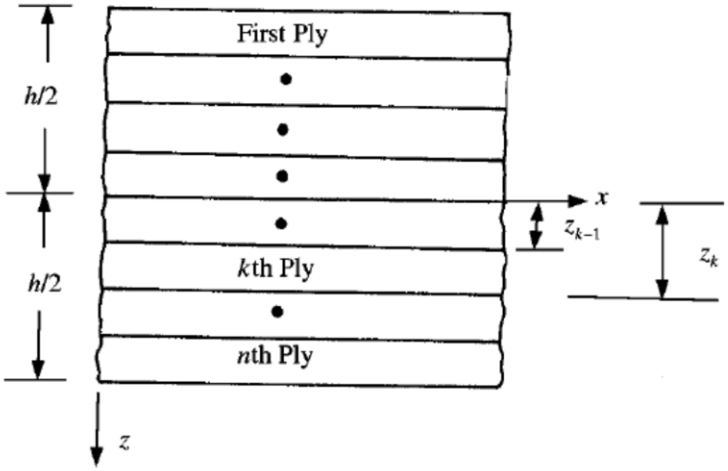

Fig 5 A typical laminate with layer details

Again, the shear rotations of the plate can be expressed as

$$\phi_x = \theta_y + w_{,x}, \quad \phi_y = -\theta_x + w_{,y} \tag{2.8}$$

The linear in-plane strains of the laminate at a distance z from the mid surface are given by

For plates,

$$\varepsilon_x = \frac{\partial u}{\partial x} = u_{,x} = \frac{\partial u^0}{\partial x} + z\frac{\partial \theta_y}{\partial x} = u^0_{,x} + z\theta_{y,x}$$
$$\varepsilon_y = \frac{\partial v}{\partial y} = v_{,y} = \frac{\partial v}{\partial y} - z\frac{\partial \theta_x}{\partial y} = v^0_{,y} - z\theta_{x,y}$$
$$\gamma_{xy} = u_{,y} + v_{,x} = u^0_{,y} + v^0_{,x} + z(\theta_{y,y} - \theta_{x,x}) \tag{2.9}$$

The above equations can be expressed as

For plates,

$$\begin{bmatrix} \varepsilon_x \\ \varepsilon_y \\ \gamma_{xy} \end{bmatrix} = \begin{bmatrix} \varepsilon^0_x \\ \varepsilon^0_y \\ \gamma^0_{xy} \end{bmatrix} + z \begin{bmatrix} k_x \\ k_y \\ k_{xy} \end{bmatrix} \tag{2.10}$$

Now

$$\begin{bmatrix} \varepsilon^0_x \\ \varepsilon^0_x \\ \gamma^0_{xy} \end{bmatrix} = \begin{bmatrix} u^0_{,x} \\ v^0_{,y} \\ u^0_{,y} + v^0_{,x} \end{bmatrix} \tag{2.11}$$

$$\begin{bmatrix} k_x \\ k_y \\ k_{xy} \end{bmatrix} = \begin{bmatrix} \theta_{y,x} \\ -\theta_{x,y} \\ \theta_{y,y} - \theta_{x,x} \end{bmatrix}$$

(2.12)

Since the transverse shear deformation is assumed same across the thickness of the laminate, γ_{xz} and γ_{yz} are identical to ϕ_x and ϕ_y, respectively

$$\gamma_{xz} = \phi_x, \gamma_{yz} = \phi_y$$

(2.13)

Substituting Eqn. in equations (2.3) and (2.4), From, Eq. (2.5a) and (2.5b), the stresses in the k[th] lamina (Fig 2.6) of a multilayered laminate can be expressed as

$$\{\sigma\}_k = [\bar{Q}]_k \{\varepsilon\}_k$$

(2.14)

By substitution of the strain variation through the thickness, Eq. 2.8, in the stress-strain relations, Eq. 2.13, the stresses in the k[th] layer can be expressed in terms of the laminate middle-surface strains and curvature as

$$\begin{bmatrix} \sigma_x \\ \sigma_y \\ \tau_{xy} \end{bmatrix}_k = \begin{bmatrix} \bar{Q}_{11} & \bar{Q}_{12} & \bar{Q}_{16} \\ \bar{Q}_{12} & \bar{Q}_{22} & \bar{Q}_{26} \\ \bar{Q}_{16} & \bar{Q}_{26} & \bar{Q}_{66} \end{bmatrix}_k \left[\begin{bmatrix} \varepsilon_x^0 \\ \varepsilon_y^0 \\ \gamma_{xy}^0 \end{bmatrix} + z \begin{bmatrix} \kappa_x \\ \kappa_y \\ \kappa_{xy} \end{bmatrix} \right]$$

(2.15)

The resultant forces and moments acting on the laminate are obtained by integration of the stresses in each layer or lamina through the laminate thickness, for example,

$$N_x = \int_{-t/2}^{-t/2} \sigma_x dz, M_x = \int_{-t/2}^{-t/2} \sigma_x z dz,$$

(2.16)

where, N_x and M_x are the force and moment per unit width of the cross section of the laminate (**Fig. 6**)

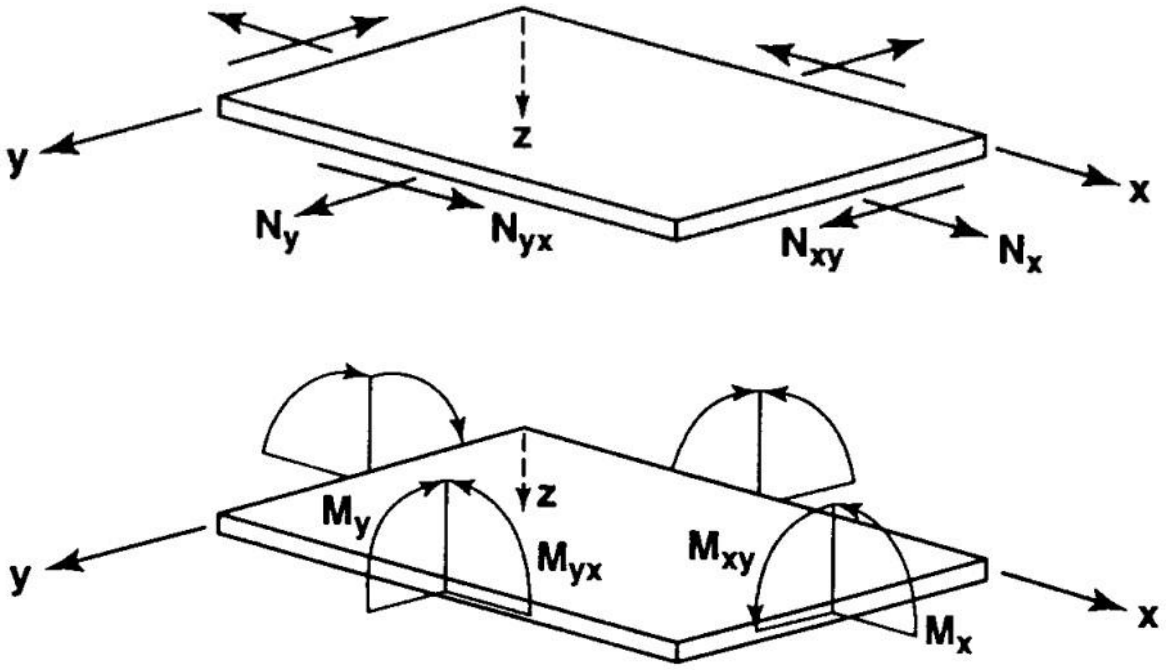

Fig. 6 In-plane Forces & Moments on a Flat Laminate

N_x and M_x for the entire laminate is obtained upon integration over the entire laminate,

$$\begin{bmatrix} N_x \\ N_y \\ N_{xy} \end{bmatrix} = \int_{-t/2}^{t/2} \begin{bmatrix} \sigma_x \\ \sigma_y \\ \tau_{xy} \end{bmatrix} dz = \sum_{k=1}^{N} \int_{z_{k-1}}^{z_k} \begin{bmatrix} \sigma_x \\ \sigma_y \\ \tau_{xy} \end{bmatrix}_k dz$$

(2.17a)

$$\begin{bmatrix} M_x \\ M_y \\ M_{xy} \end{bmatrix} = \int_{-t/2}^{t/2} \begin{bmatrix} \sigma_x \\ \sigma_y \\ \tau_{xy} \end{bmatrix} z dz = \sum_{k=1}^{N} \int_{z_{k-1}}^{z_k} \begin{bmatrix} \sigma_x \\ \sigma_y \\ \tau_{xy} \end{bmatrix}_k z dz$$

(2.17b)

where $z_k$and z_{k-1} are defined in the basis laminate geometry in **Fig. 6**. These forces and moment resultants do not depend on z after integration, but are functions of x and y, the coordinates in the plane of the laminate middle surface.

Taking advantage of the fact that the stiffness matrix for a lamina is often constant within the lamina (unless the lamina has temperature dependent or moisture dependent properties and a temperature or moisture gradient exists across the lamina). If the elevated temperature and moisture are constant through the thickness of the lamina, then the values of $[\overline{Q_{ij}}]$ are constant in the layer. Thus, the stiffness matrix goes outside the integration over each layer, but is within the summation of force and moment resultants for each layer.

When the lamina stress-strain relations (Eq.2.15) are substituted, the forces and moments become

$$\begin{bmatrix} N_x \\ N_y \\ N_{xy} \end{bmatrix} = \sum_{k=1}^{N} \begin{bmatrix} \bar{Q}_{11} & \bar{Q}_{12} & \bar{Q}_{16} \\ \bar{Q}_{12} & \bar{Q}_{22} & \bar{Q}_{26} \\ \bar{Q}_{16} & \bar{Q}_{26} & \bar{Q}_{66} \end{bmatrix}_k \left[\int_{z_{k-1}}^{z_k} \begin{bmatrix} \varepsilon_x^0 \\ \varepsilon_y^0 \\ \gamma_{xy}^0 \end{bmatrix} dz + \int_{z_{k-1}}^{z_k} \begin{bmatrix} \kappa_x \\ \kappa_y \\ \kappa_{xy} \end{bmatrix} z dz \right]$$

$$\begin{bmatrix} M_x \\ M_y \\ M_{xy} \end{bmatrix} = \sum_{k=1}^{N} \begin{bmatrix} \bar{Q}_{11} & \bar{Q}_{12} & \bar{Q}_{16} \\ \bar{Q}_{12} & \bar{Q}_{22} & \bar{Q}_{26} \\ \bar{Q}_{16} & \bar{Q}_{26} & \bar{Q}_{66} \end{bmatrix}_k \left[\int_{z_{k-1}}^{z_k} \begin{bmatrix} \varepsilon_x^0 \\ \varepsilon_y^0 \\ \gamma_{xy}^0 \end{bmatrix} z dz + \int_{z_{k-1}}^{z_k} \begin{bmatrix} \kappa_x \\ \kappa_y \\ \kappa_{xy} \end{bmatrix} z^2 dz \right]$$

(2.18)

Recalling that $\varepsilon_x^0, \varepsilon_y^0, \varepsilon_z^0, \kappa_x, \kappa_y, \kappa_{xy}$ are not functions of z, but are middle surface values so they can be removed from the summation. Hence Eq. 2.14 can be written as

$$\begin{bmatrix} N_x \\ N_y \\ N_{xy} \end{bmatrix} = \begin{bmatrix} A_{11} & A_{12} & A_{16} \\ A_{12} & A_{22} & A_{26} \\ A_{16} & A_{26} & A_{66} \end{bmatrix} \begin{bmatrix} \varepsilon_x^0 \\ \varepsilon_y^0 \\ \gamma_{xy}^0 \end{bmatrix} + \begin{bmatrix} B_{11} & B_{12} & B_{16} \\ B_{12} & B_{22} & B_{26} \\ B_{16} & B_{26} & B_{66} \end{bmatrix} \begin{bmatrix} \kappa_x \\ \kappa_y \\ \kappa_{xy} \end{bmatrix}$$

$$\begin{bmatrix} M_x \\ M_y \\ M_{xy} \end{bmatrix} = \begin{bmatrix} B_{11} & B_{12} & B_{16} \\ B_{12} & B_{22} & B_{26} \\ B_{16} & B_{26} & B_{66} \end{bmatrix} \begin{bmatrix} \varepsilon_x^0 \\ \varepsilon_y^0 \\ \gamma_{xy}^0 \end{bmatrix} + \begin{bmatrix} D_{11} & D_{12} & D_{16} \\ D_{12} & D_{22} & D_{26} \\ D_{16} & D_{26} & D_{66} \end{bmatrix} \begin{bmatrix} \kappa_x \\ \kappa_y \\ \kappa_{xy} \end{bmatrix}$$

(2.19)

Where,

$$A_{ij} = \sum_{k=1}^{N} (\bar{Q}_{ij})_k (z_k - z_{k-1})$$

$$B_{ij} = \frac{1}{2} \sum_{k=1}^{N} (\bar{Q}_{ij})_k (z_k^2 - z_{k-1}^2)$$

$$D_{ij} = \frac{1}{3} \sum_{k=1}^{N} (\bar{Q}_{ij})_k (z_k^3 - z_{k-1}^3)$$

(2.20)

Combining the above relations (Eq. 2.16 and 2.17) and including the transverse shear resultants, the in-plane stress resultants $\{N\}$, the moments resultants $\{M\}$, and the transverse shear resultants $\{Q\}$, are related to the midplane strains and curvatures for a general laminated shell element as

$$\begin{Bmatrix} N_x \\ N_y \\ N_{xy} \\ M_x \\ M_y \\ M_{xy} \\ Q_y \\ Q_x \end{Bmatrix} = \begin{bmatrix} A_{11} & A_{12} & A_{16} & B_{11} & B_{12} & B_{16} & 0 & 0 \\ A_{12} & A_{22} & A_{26} & B_{12} & B_{22} & B_{26} & 0 & 0 \\ A_{16} & A_{26} & A_{66} & B_{16} & B_{26} & B_{66} & 0 & 0 \\ B_{11} & B_{12} & B_{16} & D_{11} & D_{12} & D_{16} & 0 & 0 \\ B_{12} & B_{22} & B_{26} & D_{12} & D_{22} & D_{26} & 0 & 0 \\ B_{16} & B_{26} & B_{66} & D_{16} & D_{26} & D_{66} & 0 & 0 \\ 0 & 0 & 0 & 0 & 0 & 0 & A_{44} & A_{45} \\ 0 & 0 & 0 & 0 & 0 & 0 & A_{45} & A_{55} \end{bmatrix} \begin{Bmatrix} \varepsilon_{xx}^0 \\ \varepsilon_{yy}^0 \\ \gamma_{xy}^0 \\ k_x \\ k_y \\ k_{xy} \\ \gamma_{yz} \\ \gamma_{xz} \end{Bmatrix}$$

(2.21a)

Where, N_x, $N_y$and N_{xy} are in-plane stress resultants, M_x, $M_y$and M_{xy} are moment resultants and Q_x, Q_y are transverse shear stress resultants.

In short,

$$\{N\} = [A]\{\varepsilon^0\} + [B]\{\kappa\}$$
$$\{M\} = [B]\{\varepsilon^0\} + [D]\{\kappa\}$$
$$\{Q\} = [A^*]\{\gamma\}$$

(2.21b)

where, [A], [B] and [D] are the stiffness coefficients.

The extensional, bending-stretching and bending stiffnesses of the laminate are expressed in the usual form as

$$(A_{ij},\, B_{ij},\, D_{ij}) = \sum_{k=1}^{n} \int_{Z_{k-1}}^{Z_k} (\bar{Q}_{ij})_k (1, z, z^2)\, \mathrm{d}z, \quad i,j = 1,2,6.$$

(2.21c)

Similarly, the shear stiffness is expressed as

$$\left(A_{ij}^*\right) = \sum_{k=1}^{n} \int_{z_{k-1}}^{z_k} \alpha(\bar{Q}_{ij})_k dz, i,\, j = 4,5$$

(2.21d)

α, the shear correction factor which is derived from the Timoshenko beam concept by applying the energy principle and is assumed as 5/6. It accounts for the non-uniform distribution of transverse shear stress across the thickness of the laminate.

2.4 *FINITE ELEMENT FORMULATION*

The finite element formulations and the solution details are presented here. An eight nodedisoparametric element is employed, both the geometry and displacement field of which are expressed in terms of the same shape functions. The parent element in local natural coordinate system can be mapped to an arbitrary shape in the Cartesian coordinate system.

2.4.1*QUADRATIC ISOPARAMETRIC ELEMENT*

Consider an eight node isoparametric element Figs 2.7(a) & (b) with five degrees of freedom at each node, viz. $u^0, v^0, w^0, \theta_x, \theta_y$. The element geometry and displacement field are expressed by the quadratic shape functions (N_i).

$$x = \sum_{i=1}^{8} N_i x_i \qquad y = \sum_{i=1}^{8} N_i y_i$$

(2.22)

Where x_i and y_i are the global coordinate at a node i.

By using the eight-noded element shape functions, the element displacements are expressed in terms of their nodal values given by

$$u^0 = \sum_{i=1}^{8} N_i u_i^0, \quad v^0 = \sum_{i=1}^{8} N_i v_i^0, \quad w = \sum_{i=1}^{8} N_i w_i, \quad \theta_x = \sum_{i=1}^{8} N_i \theta_{xi}, \quad \theta_y = \sum_{i=1}^{8} N_i \theta_{yi}$$

(2.23)

where N_i*'s* are the shape functions used to interpolate the generalized displacements, u_i^0, v_i^0, w_i,θ_{xi}, θ_{yi} at node *I* within an element.

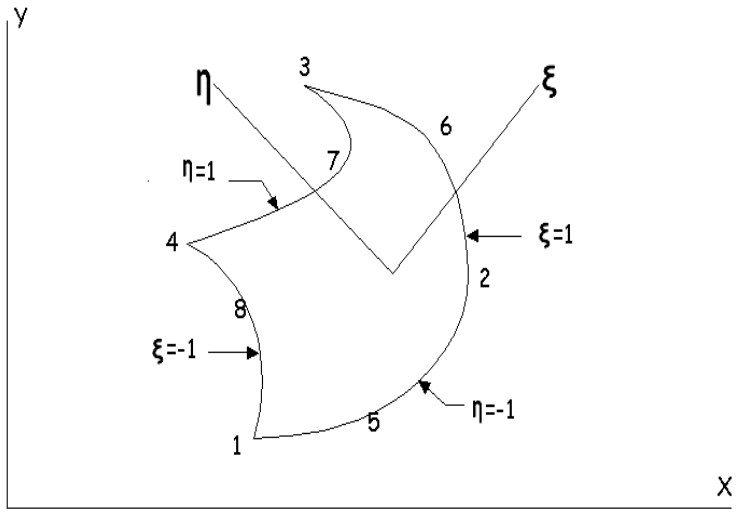

Fig. 7(a) Mapping of the element in X-Y plane

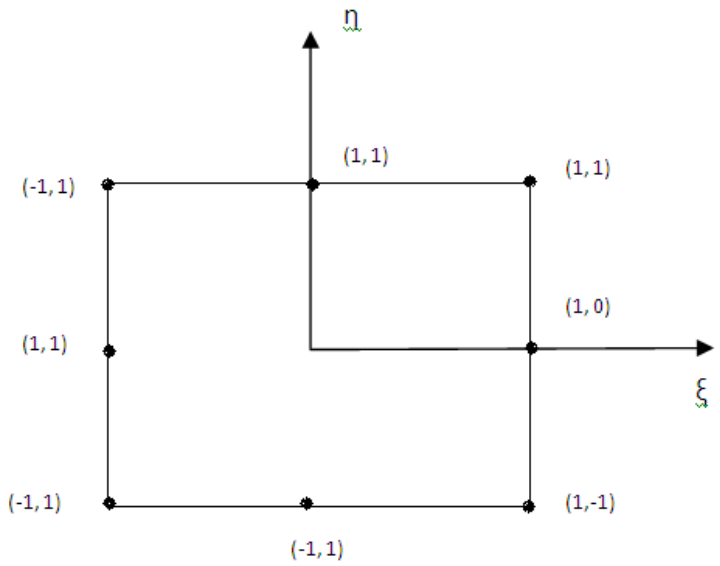

Fig 7(b) The element in the ξ – η space

An eight noded isoparametric quadratic plate bending element with five degrees of freedom at each node (three translations and two rotations) is considered wherein the shape functions are given as

$$N_i = (1+\xi\xi_i)(1+\eta\eta_i)(\xi\xi_i+\eta\eta_i-1)/4 \cdots\cdots i = 1,2,3,4$$
$$N_i = (1-\xi^2)(1+\eta\eta_i)/2 \cdots\cdots i = 5,7$$
$$N_i = (1-\eta^2)(1+\xi\xi_i)/2 \cdots\cdots i = 6,8$$

(2.24)

Where, ξ and η are the local natural coordinates of the element and ξ_i and η_i are the values at a node "*i*", *i* ranges from 1 to 8.

$$\begin{bmatrix} N_{i,x} \\ \\ N_{i,y} \end{bmatrix} = [J]^{-1} \begin{bmatrix} N_{i,\xi} \\ \\ N_{i,\eta} \end{bmatrix}$$

$$[J] = \begin{bmatrix} x_{,\xi} & y_{,\xi} \\ x_{,n} & y_{,n} \end{bmatrix}$$

(2.25)

where, [*J*] is the Jacobian Matrix.

2.4.2 *ELEMENT STIFFNESS MATRIX*

The potential energy of deformation for the element, is expressed as

$$U_e = \frac{1}{2}\int\int_A \{\varepsilon\}^T [D] \{\varepsilon\} dA$$

(2.26)

If $\{\varepsilon\} = [B]\{\delta_e\} = [[B_1].....[B_8]] \{\delta_e\}$

Where $\{\delta_e\} = \{\overline{u_1} \quad \overline{v_1} \quad w_1 \quad \theta_{x1} \quad \theta_{y1} .....\overline{u_8} \quad \overline{v_8} \quad w_8 \quad \theta_{x8} \quad \theta_{y8}\}^T$

(2.27)

Then,

$$U_e = \frac{1}{2}\int_{-a/2}^{a/2}\int_{-b/2}^{b/2} \{\delta_e\}^T [B]^T [D][B]\{\delta_e\} dxdy$$

$$= \frac{1}{2}\{\delta_e\}^t [K_e]\{\delta_e\}$$

(2.28)

In which,

$$[K_e] = \int_{-a/2}^{a/2}\int_{-b/2}^{b/2} [B]^T [D][B] dxdy$$

(2.29)

$[B_i]$, the Strain-Displacement Matrix in the above equation is given by

$$[B_{ii}]=\begin{bmatrix} N_{i,x} & 0 & N_i/R_x & 0 & 0 \\ 0 & N_{i,y} & N_i/R_y & 0 & 0 \\ N_{i,y} & N_{i,x} & N_i/R_{xy} & 0 & 0 \\ 0 & 0 & 0 & 0 & N_{i,x} \\ 0 & 0 & 0 & -N_{i,y} & 0 \\ 0 & 0 & 0 & -N_{i,x} & N_{i,y} \\ 0 & 0 & N_{i,x} & 0 & N_i \\ 0 & 0 & N_{i,y} & -N_i & 0 \end{bmatrix}$$

(i = 1 to 8)

For twisted plates,

$N_i/R_x = N_i/R_y = 0$

For twisted conical shells,

$N_i/R_x = 0$

Now, $dxdy = |J|d\xi d\eta$, where $[J]$ is the determinant of the Jacobian matrix, the element stiffness matrix can be expressed in local natural coordinates of the element as

$$[K_e]=\int_{-1}^{1}\int_{-1}^{1}[B]^T[D]\ [B]\ |J|\ d\xi d\eta$$

(2.30)

Where, [*B*] is the strain-displacement matrix, [*D*], the elasticity matrix and *J* is the determinant of the Jacobian matrix. Reduced integration (2X2) is employed to avoid the shear locking.

2.4.3*ELEMENT MASS MATRIX*

Similar to the case of stiffness matrix, the consistent element mass matrix $[M_e]$ is expressed as

$$[M_e] = \int_{-1}^{1}\int_{-1}^{1}[N]^{\mathrm{T}}[\rho]\,[N]J\,\mathrm{d}\xi\,\mathrm{d}\eta$$

where [N] is the shape function matrix and [ρ] is the inertia matrix.

[N] Is given by

$$[N] = [[N_1] \ldots\ldots\ldots\ldots [N_8]]$$

(2.31)

where,

$$[N_i] = \begin{bmatrix} N_i & & & & \\ 0 & N_i & & Symmetric & \\ 0 & 0 & N_i & & \\ 0 & 0 & 0 & N_i & \\ 0 & 0 & 0 & 0 & N_i \end{bmatrix}$$

(2.32)

$[M_e]$ is calculated using (2 x 2) Gauss quadrature.

2.5*DYNAMIC EQUILIBRIUM EQUATIONS*

The dynamic equilibrium equation for moderate rotational speeds is derived employing Lagrange's equation of motion and neglecting Coriolis effect the equation in global form is expressed as[60]

$$[M]\{\ddot{\delta}\} + ([K] + [K_\sigma])\{\delta\} = 0$$

(2.33)

Where, [M], [K], $[K_\sigma]$ are global mass, elastic stiffness and geometric stiffness matrices, respectively. $\{F(\Omega^2)\}$ is the nodal equivalent centrifugal forces and $\{\delta\}$ is the global displacement vector. $[K_\sigma]$ depends on the initial stress distribution and is obtained by the iterative procedure[61] upon solving

$$([K] + [K_\sigma])\{\delta\} = 0$$

(2.34)

The matrix of angular velocity components contributing towards acceleration vector is given as[60,62]

$$[A] = \begin{bmatrix} \Omega_y{}^2 + \Omega_z{}^2 & -\Omega_x\Omega_y & -\Omega_x\Omega_z \\ -\Omega_x\Omega_y & \Omega_x{}^2 + \Omega_z{}^2 & -\Omega_y\Omega_z \\ -\Omega_x\Omega_z & -\Omega_y\Omega_z & \Omega_x{}^2 + \Omega_y{}^2 \end{bmatrix}$$

(2.35)

The element geometric stiffness matrix due to rotation is given by

$$[K_{\sigma\varepsilon}] = \int_{vol} [G]^T [M_\sigma][G]\, d(vol)]$$

(2.36)

Where, the matrix [G] consists of derivatives of shape functions and $[M_\sigma]$ is the matrix of initial in-plane stress resultants caused by rotation.

The natural frequencies are determined from the standard eigenvalue problem which is represented below and is solved by QR iteration algorithm.

$$[A]\{\delta\} = \lambda\{\delta\}$$

$$\text{where } [A] = ([K] + [K_\sigma])^{-1}[M] \text{ and } \lambda = 1/\omega_n{}^2$$

(2.37)

IMPACT MODELLING ON FGM PLATES

The dynamic equilibrium equation is given by

$$[\mathbf{M}]\{\ddot{\boldsymbol{\delta}}\} + [\mathbf{K}]\{\boldsymbol{\delta}\} = \{\mathbf{F_C}\} \qquad (\mathbf{26})$$

The contact force vector {F} is given by

$\{F\} = \{0\ 0\ 0\ \ldots\ldots F_{c\ldots\ldots}\ 0\ 0\ 0\}$, For single-site impact

The equation of motion for each rigid impactor is given by

$$\mathbf{m_i}\ddot{\boldsymbol{\delta}}_\mathbf{i} + \mathbf{F_c} = \mathbf{0} \qquad (\mathbf{27})$$

The Newmark's constant acceleration time integration scheme is used in solving the equations of motion of the shell and impactors.

CONTACT FORCE

The contact force during loading

$$\mathbf{F_c} = \mathbf{k}\boldsymbol{\alpha}^{\mathbf{1.5}},\ \mathbf{0} < \boldsymbol{\alpha} < \boldsymbol{\alpha}_\mathbf{m} \qquad (\mathbf{28})$$

The contact stiffness k is given by the following expression

$$\mathbf{k} = \frac{4}{3}\sqrt{\mathbf{r_i}}\frac{1}{\frac{1-\gamma_i^2}{E_1}+\frac{1}{E_2}} \qquad (29)$$

The contact force F_c for unloading and reloading are given by

$$\mathbf{F_c} = \mathbf{F_m}\left[\frac{\alpha-\alpha_0}{\alpha_m-\alpha_0}\right]^{2.5} \text{ and } \quad \mathbf{F_c} = \mathbf{F_m}\left[\frac{\alpha-\alpha_0}{\alpha_m-\alpha_0}\right]^{1.5} \qquad (30)$$

The local indentation at the indentation point is given by

$$\boldsymbol{\alpha(t) = w_i - w_p \cos\psi} \qquad (31)$$

SET-UP FOR PRESENT WORK

A simply-supported FGM plate with dimensions of (20×20×0.269) cm is considered. The elastic properties of impactor (steel ball) and FGM plate as adopted by Zhao et al. (??) are mentioned in **Table 1**. The plates are assumed to be impacted at the center by a spherical steel ball of 1.27 cm diameter. The mass density of the impactor is 7860 kg/m^3. Consider the plate is impacted centrally by a spherical impactor at the middle of the span length $(\frac{a}{2}, \frac{b}{2})$ with different initial impactor velocities (i.e. 1.0 m/sec, 2.0m/sec and 3.0m/sec). For these combinations of metal and ceramic different combinations of power index (*k*) were used such as 0, 2, 5 and 10. Different value of power index will lead different stiffnesses of the FGM plate that in turn causes changes in the contact force, plate and impactor displacement and impactor velocities. These combinations of initial VOI (velocity of Impact), power index and different metallic and ceramic constituent combinations are used to generate the transient response of FGM plates and are plotted and analyzed. The FGM combinations of Al/Al_2O_3, Ti–6Al–4V/Aluminum oxide, SUS304/Si_3N_4 and Al/ZrO_2 are used as combinations of metal and ceramic constituents for analyses. A converged time step of 2 micro-second is used in FEM codes and generated graphs are plotted for time-range unto which the contact forces reduces to zero after which the changes in the plate and impactor displacement and imactor velocities may be assumed to be insignificant.

MATERIAL PROPERTIES OF FGM PLATE (Zhao et al. [??])

Material	Elastic modulus, E (N/m^2)	Poisson ratio (ϑ)	Density, ρ (kg/m^3)
Aluminum(Al)	$70.0x10^9$	0.30	2707
Alumina (Al_2O_3)	$380.0x10^9$	0.30	3800
Zirconia (ZrO_2)	$151x10^9$	0.30	3000
Ti-6Al-4V	$105.7x10^9$	0.298	4429
Aluminum Oxide	$320.2x10^9$	0.26	3750
Stainless Steel SUS304	$207.78x10^9$	0.3177	8166
Silicon nitride Si_3N_4	$322.27x10^9$	0.24	2370

From above table, the various combinations of Metal/Ceramic comprising the FGM as considered are mentioned below-

METAL	CERAMIC
Aluminum(Al)	Alumina(Al_2O_3)
Aluminum(Al)	Zirconia (ZrO_2)
Ti-6Al-4V	Aluminum Oxide
Stainless Steel SuS_3O_4	Silicon nitride Si_3N_4

Validation Of The Computer Codes

The present FEM codes are initially validated with the established results of impact behavior of both steel plates and FGM materials. The contact force obtained for the impact of a steel ball on a steel plate is validated in **Fig. 8** by the present FEM code with the works of Karas (1939) and Wu et al. (1989). In this case, a square steel plate is assumed to be impacted by a spherical steel ball at the center under simply-supported boundary conditions. The details of the problem and the material properties are given below:

$a=b=0.2$, $VOI=1$m/s, $E=206$GPa.

Again, the present work is validated with the transient response of FGM plates with constituents as Silicon nitride and stainless steel as performed by Kiani et al. [??] and presented in **Fig. 9**. The validation is done considering a beam of dimensions a=153.5mm, b=15mm and thickness *h*=10mm. The impactor velocity is VOI=1m/s, radius R=0.0127m, mass of impactor =10gm while the power law index is assumed to be k=1.0. The close agreement of the present FEM results with the published works establishes the accuracy and suitability of the present finite element formulation in accurately predicting the transient response behavior of FGM plates with varied constituents.

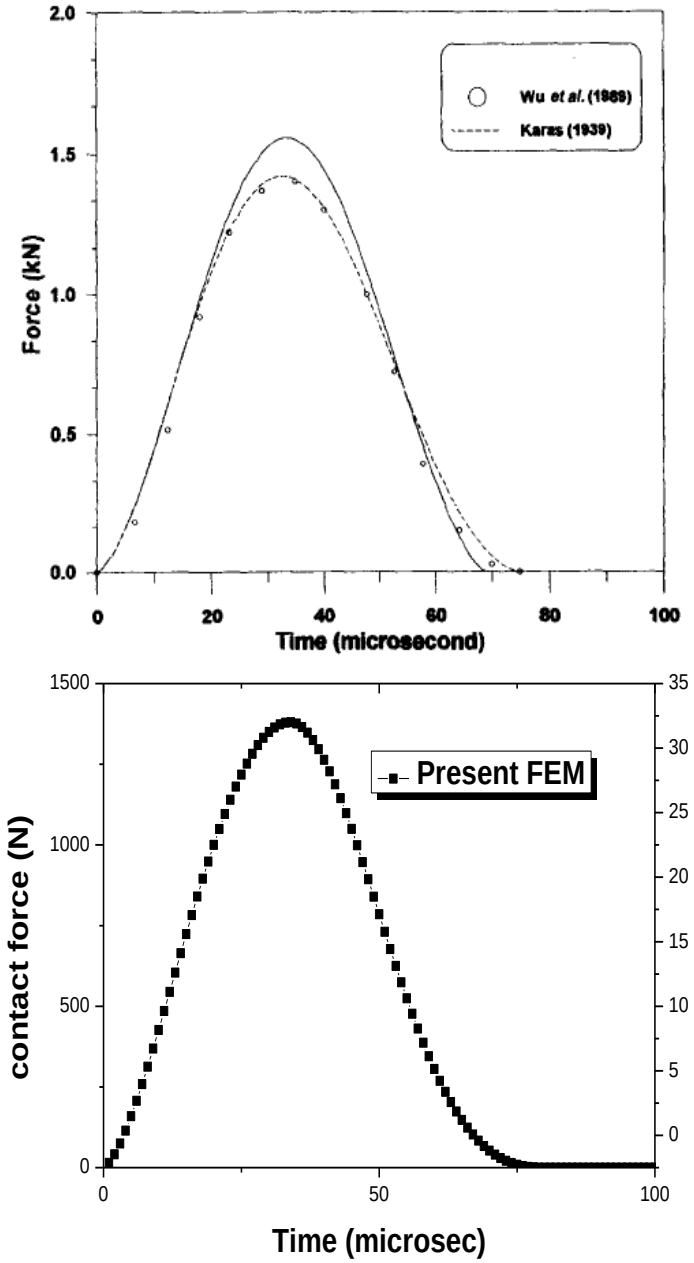

Fig. 8: Validation of the present FEM with the transient response of impact on steel plates by Karas (1939) and Wu et al. (1989)

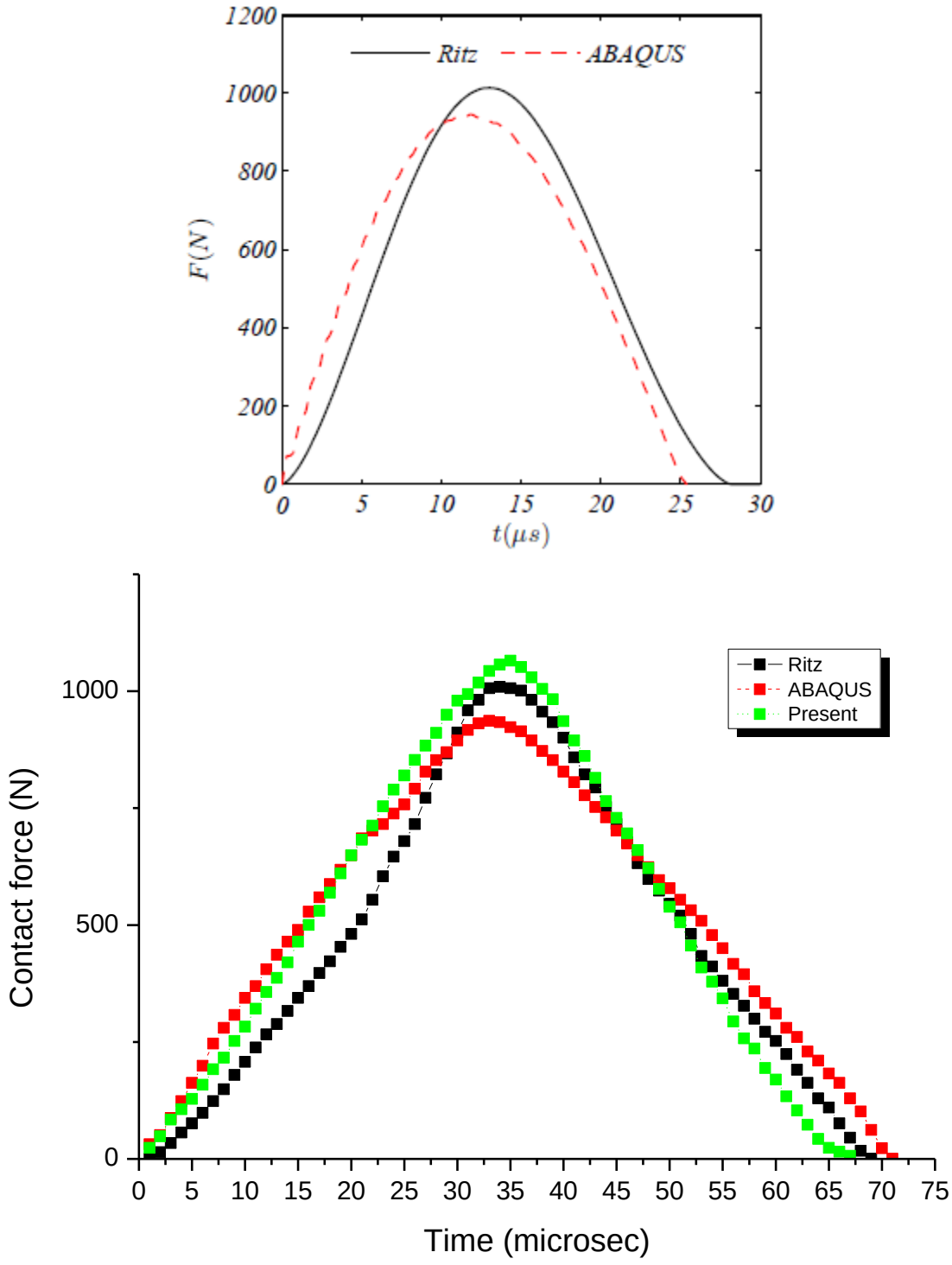

Fig. 9 Validation of the present FEM with the transient response of FGM plates under impact (Kiani et al. [??])

RESULTS AND DISCUSSIONS

The impact behavior (contact force and impactor displacements) of FGM plates for a power index (k) = 0.0 are plotted and presented in **Fig 10. (a)** and **10(b)** for Al/Al_2O_3 and Al/ZrO_2 FGM plates for different values of the impactor velocities (VOI). It is observed that the pattern of variations of the contact force and the impactor displacements are almost similar for both the FGM combinations (Al/Al_2O_3 and Al/ZrO_2) considered. It is noted that there is a drastic increase in the contact force values with an increase in the impactor velocities (VOI). This may be directly attributed to the increase in the initial kinetic energy of the spherical impactor that results in a large contact force for the FGM plate. The impactor displacement values are found to first increase then decrease attaining negative displacements suggesting that the impactor tends to move in the opposite direction. Owing to the slowing down of the impactors, no reloading curves are observed in case of impact on the FGM plates for the configurations considered. At VOI=3m/s, For Al/Al_2O_3, The Maximum value of contact force is 1158N at time-step of 50 μs and its decreases afterwards. For Al/ZrO_2 contact force attains maximum value of 1120 N at the time-steps 42 μs and it decrease afterwards. The impactor displacement attains the peak value (0.09 mm) in time-steps of 50 μs for both Al/Al_2O_3andAl/ZrO_2. At VOI=2m/s, For Al/Al_2O_3, The Maximum value of contact force is 710N at time-steps of 52 μs and its decreases afterwards. For Al/ZrO2 contact force attains maximum value of 688 N time-steps of 50μs and it decrease afterwards. The impactor displacement is increasing from 0 to the peak value (0.065 mm) in time-steps of 52 μs for both $Al/Al_2O_3$and Al/ZrO2 and is decreases afterwards. At VOI=1m/s, For Al/Al_2O_3contacts force attains maximum value of 307N at time-steps of 54 μs and its decreases afterwards. For Al/ZrO2 contact force attains maximum value of 299 N at the time-steps of 56 μs and it decrease afterwards. The impactor displacement attains the peak value (0.037 mm) in time 54 μs for both $Al/Al_2O_3$and Al/ZrO2and is decreases afterwards.

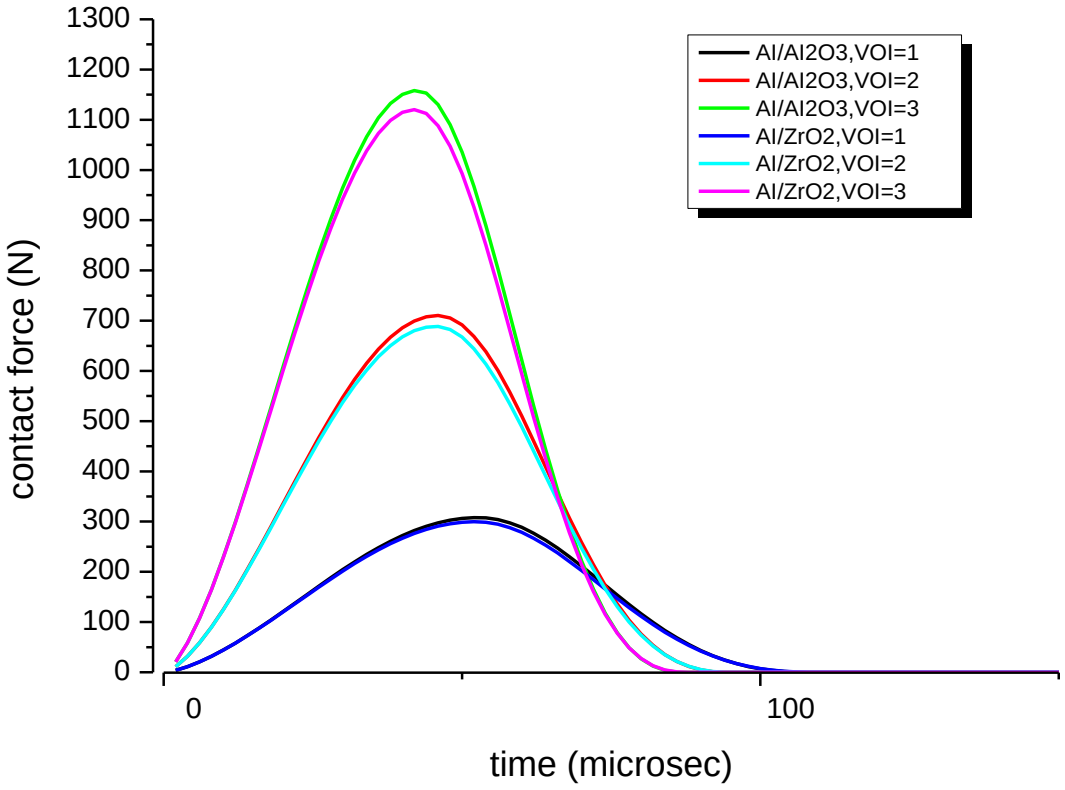

Fig.10(a) Plot For Contact Force Vs. Time-Step For The Power Factor (K)=0

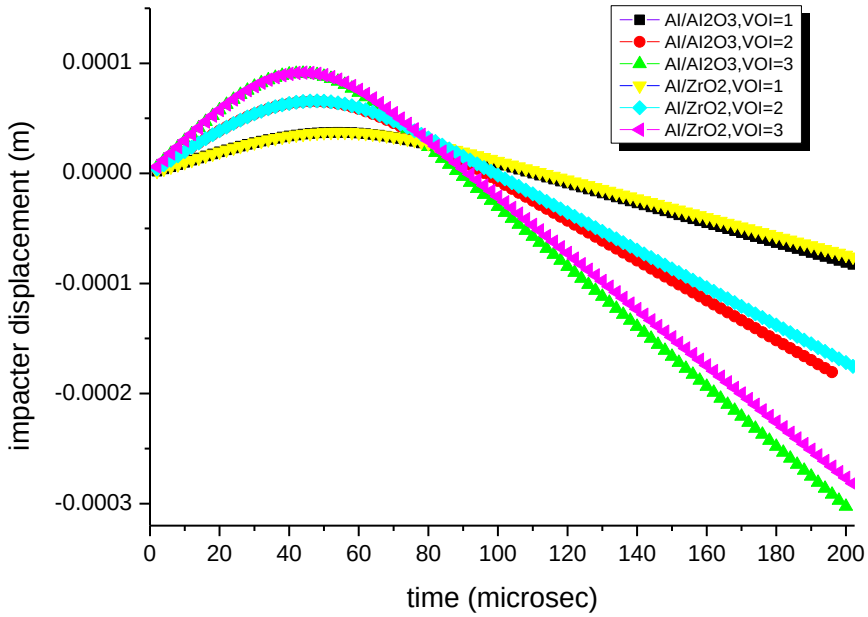

Fig.10(b) Plot For Impactor Displacement vs. Time-Step For The Power Factor (k)=0

The impact behavior (plate displacements and impactor velocities) of FGM plates for a power index (k) = 0.0 are plotted and presented in **Fig. 11(a)** and **11(b)** for Al/Al_2O_3 and Al/ZrO_2 FGM plates for different values of the impactor velocities (VOI). An increase in the plate displacement is generally observed with an increase in the impactor velocity (VOI) which may be attributed to the higher energy imparted on the FGM plate with an increase in the impactor velocity. As the impactor gradually losses energy after the impact, the impactor velocity is observed to decrease gradually with an increase in the time-step. The impactor velocity becomes zero close to the time-step of t=50μs, where the maximum value of the contact force is observed indicating that the contact force reaches its maximum value where the impactor velocity changes its sign. In addition, the impactor velocity attains a negative value after this range indicating that the impactor now moves in an opposite direction compared to the plate displacement resulting in separation of the plate and the impactor. At VOI=3m/s, the impactor velocity for both Al/Al2O3& Al/ZrO2 starts from 3 m/s and it decreases sharply to attains value of -2.72m/s for Al/Al2O3and - 2.5m/s for Al/ZrO2 at time 90 μs. Plate displacement for attains first maxima of 2mm at time-step of 74 μs then further rises to second maxima of 2.67mm at time 164 μs. For Al/ZrO2 attains first maxima of 3.8mm at 80 μs then further rises to a maximum of 4.9 mm at time of 206 μs. At VOI=2m/s, the impactor velocity for both Al/Al2O3 and Al/ZrO2 starts from 2 m/s and it decreases sharply to attains value of -1.81m/s for and - 1.5m/s for Al/ZrO2 at time 100 μs. and 96 μs. Plate displacement for Al/Al2O3 attains first maxima of 1.3 mm at time-step of 80 μs then further rises to second maxima of 1.74 mm at time 164 μs. For Al/ZrO2 attains first maxima of 2.5mm at 80 μs then further rises to second maxima of 3.2 mm at time of 200 μs. At VOI=1m/s, the impactor velocity for both Al/Al2O3 & Al/ZrO2 starts from 1m/s and it decreases sharply to attains value of -0.9 m/s for Al/Al2O3 and 0.85 m/s for Al/ZrO2 at time 106 μs. Plate displacement for Al/Al2O3attains first maxima of .6mm at time-step of 80 μs then further rises to second maxima of 0.84mm at time 168 μs. For Al/ZrO2 attains first maxima of 1mm at 100 μs then further rises to second maxima of 1.5 mm at time of 200 μs.

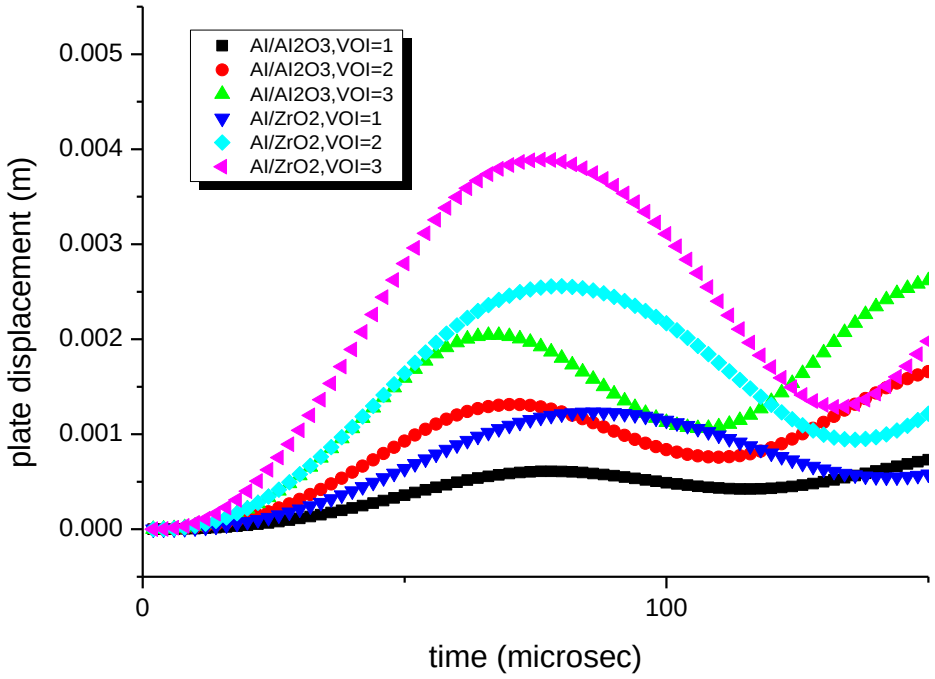

Fig.11(a) Plot For Plate Displacement Vs time-Step For Power Factor (k)=0

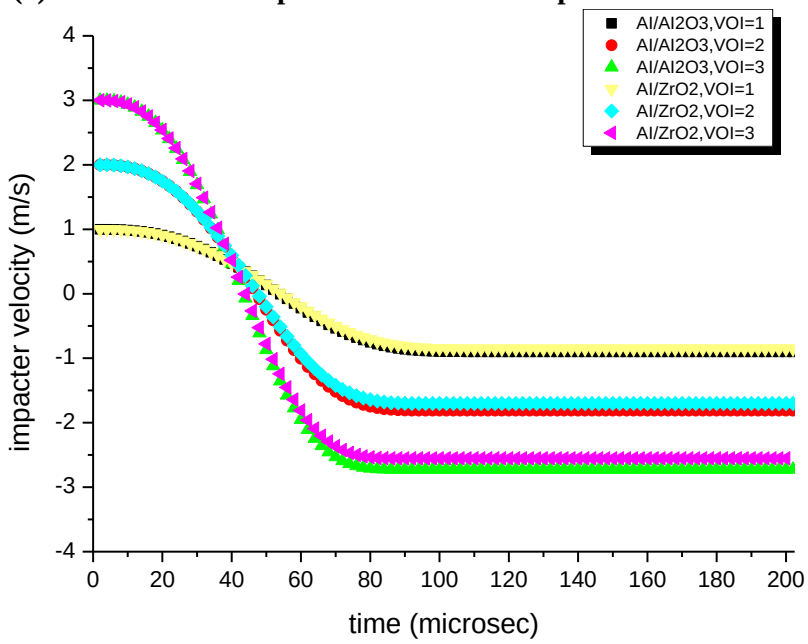

Fig.11(b) Plot For Impactor Velocity Vs. Time-Step For Power Factor (k)=0

RESULT OF CONTACT FORCE & IMPACTOR DISPLACEMENT FOR (K)= 2

The impact behavior (contact force and impactor displacements) of FGM plates for a power index (k) = 2.0 are plotted and presented in **Fig 12(a)** and **12(b)** for Al/Al_2O_3 and Al/ZrO_2 FGM plates for different values of the impactor velocities (VOI). At VOI=3m/s, for Al/Al2O3, the maximum value of contact force is 1100N at a time-step of 45 μs and then decreases afterwards. For Al/ZrO2 contact force attains maximum value of 1050 N at the time-steps 50 μs and it decrease afterwards. The impactor displacement attains the peak value (0.10 mm) in time-steps of 50 μs for both Al/Al_2O_3andAl/ZrO2. At VOI=2m/s, For Al/Al_2O_3, the Maximum value of contact force is 650N at time-steps of 50 μs and its decreases afterwards. For Al/ZrO2 contact force attains maximum value of 674 N at time-steps of 45μs and it decrease afterwards. The impactor displacement is increasing from 0 to the peak value (0.05 mm) in time-steps of 45 μs for both $Al/Al_2O_3$and Al/ZrO2 and is decreases afterwards. At VOI=1m/s, For Al/Al_2O_3, the contacts force attains maximum value of 299N at time-steps of 50 μs and its decreases afterwards. For Al/ZrO2 contact force attains maximum value of 294 N at the time-steps of 50 μs and it decrease afterwards. The impactor displacement attains the peak value (0.037 mm) in time-steps of 55 μs for both $Al/Al_2O_3$and Al/ZrO2 and is decreases afterwards.

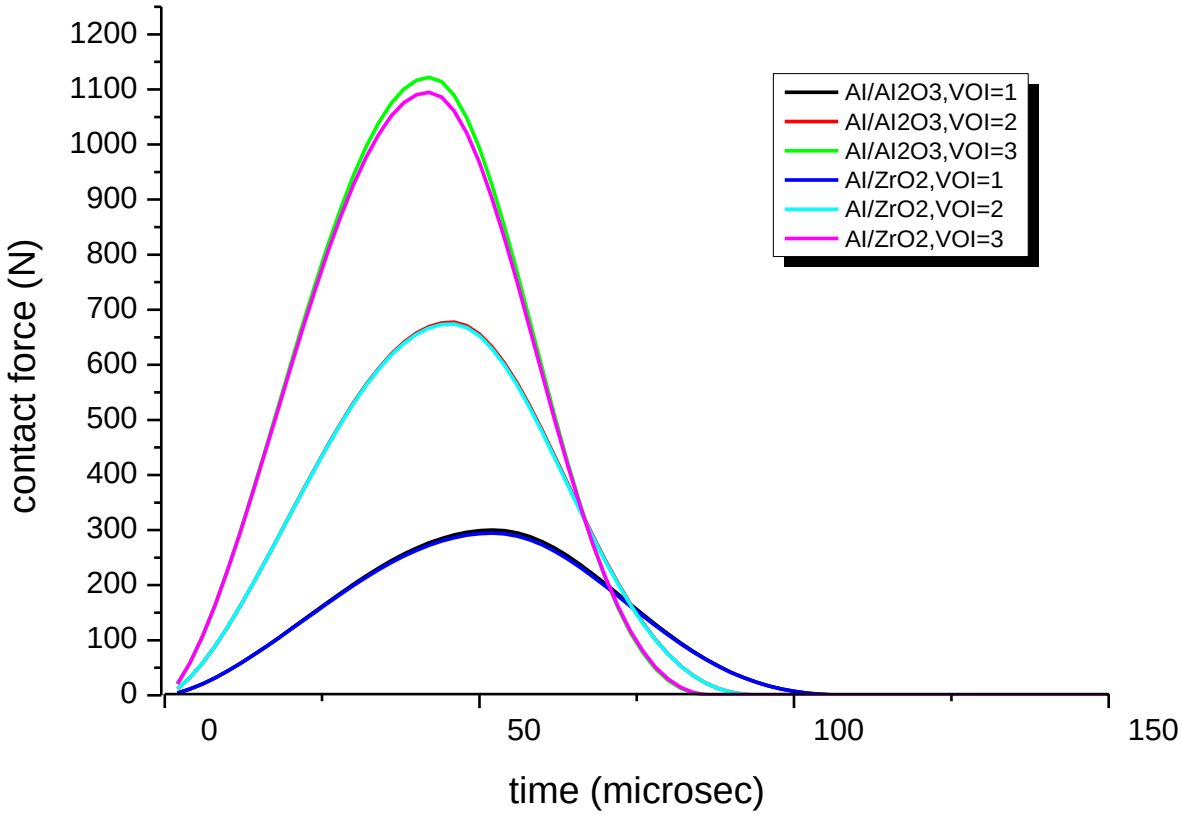

Fig. 12(a) Plot For Contact Force Vs. Time - Step For The Power Factor (K)=2

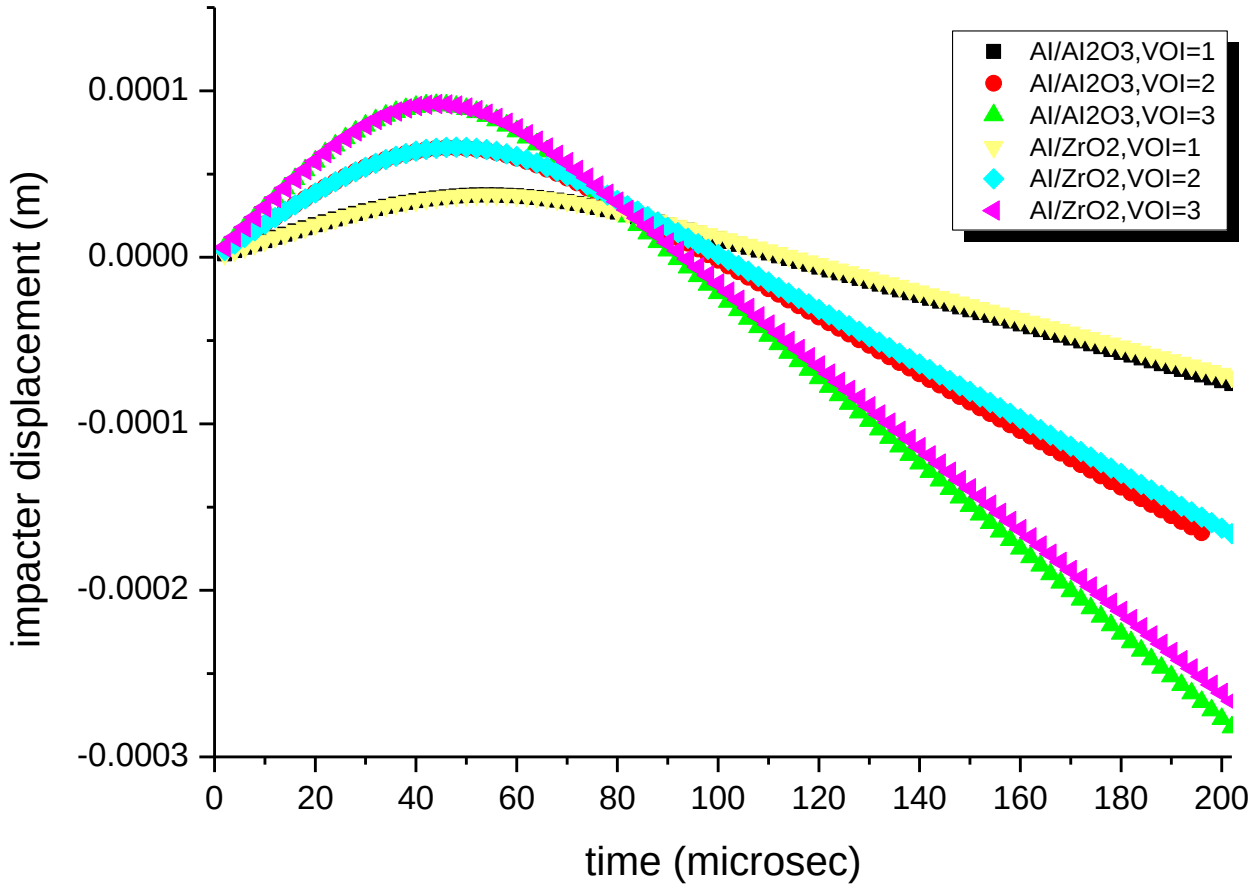

Fig. 12(b) Plot For Impactor Displacement Vs Time-Step For The Power Factor (*k*)=2

RESULT OF IMPACTOR VELOCITY & PLATE DISPLACEMENT FOR (*k*) = 2

The impact behavior (plate displacements and impactor velocities) of FGM plates for a power index (*k*) = 2.0 are plotted and presented in **Fig. 13(a)** and **13(b)** for Al/Al_2O_3 and Al/ZrO_2 FGM plates for different values of the impactor velocities (VOI). At VOI=3m/s, the impactor velocity for both Al/Al_2O_3 & Al/ZrO2 starts from 3 m/s and it decreases sharply to attains value of -2.55m/s for both $Al/Al_2O_3$and Al/ZrO2 at time 80 µs. Plate displacement for Al/Al_2O_3attains first maxima of 3.8mm at time-step of 80 µs then further rises to second maxima of 4.9 mm at time 200 µs. For Al/ZrO2 attains first maxima of 5mm at 100 µs then to a lower dip at 150 microseconds and further rises to a maximum of 7mm at time of 250 µs. At VOI=2m/s, the impactor velocity for both Al/Al_2O_3& Al/ZrO2 starts from 2m/s and it decreases sharply to attains value of -1.7 m/s for both Al/Al2O3and Al/ZrO2 at time 85 µs. Plate displacement for Al/Al_2O_3attains first maxima of 2.5mm at time-step of 80µs then further rises to second maxima of 3mm at time 200 µs. For Al/ZrO2 attains first maxima of 2.5mm at 80 µs then further rises to second maxima of 4.8 mm at time of 250 µs. At VOI=1m/s, the impactor velocity for both Al/Al_2O_3& Al/ZrO2 starts from 1 m/s and it decreases sharply to attains value of -0.82m/s for both $Al/Al_2O_3$and Al/ZrO2 at time 100 µs. Plate displacement for Al/Al_2O_3attains first maxima of 1.2 mm at time-step of 84 µs then further rises to second maxima of 1.5mm at time 210 µs. For Al/ZrO2 attains first maxima of 1.64mm at 100 µs then further rises to second maxima of 2 mm at time of 200 µs.

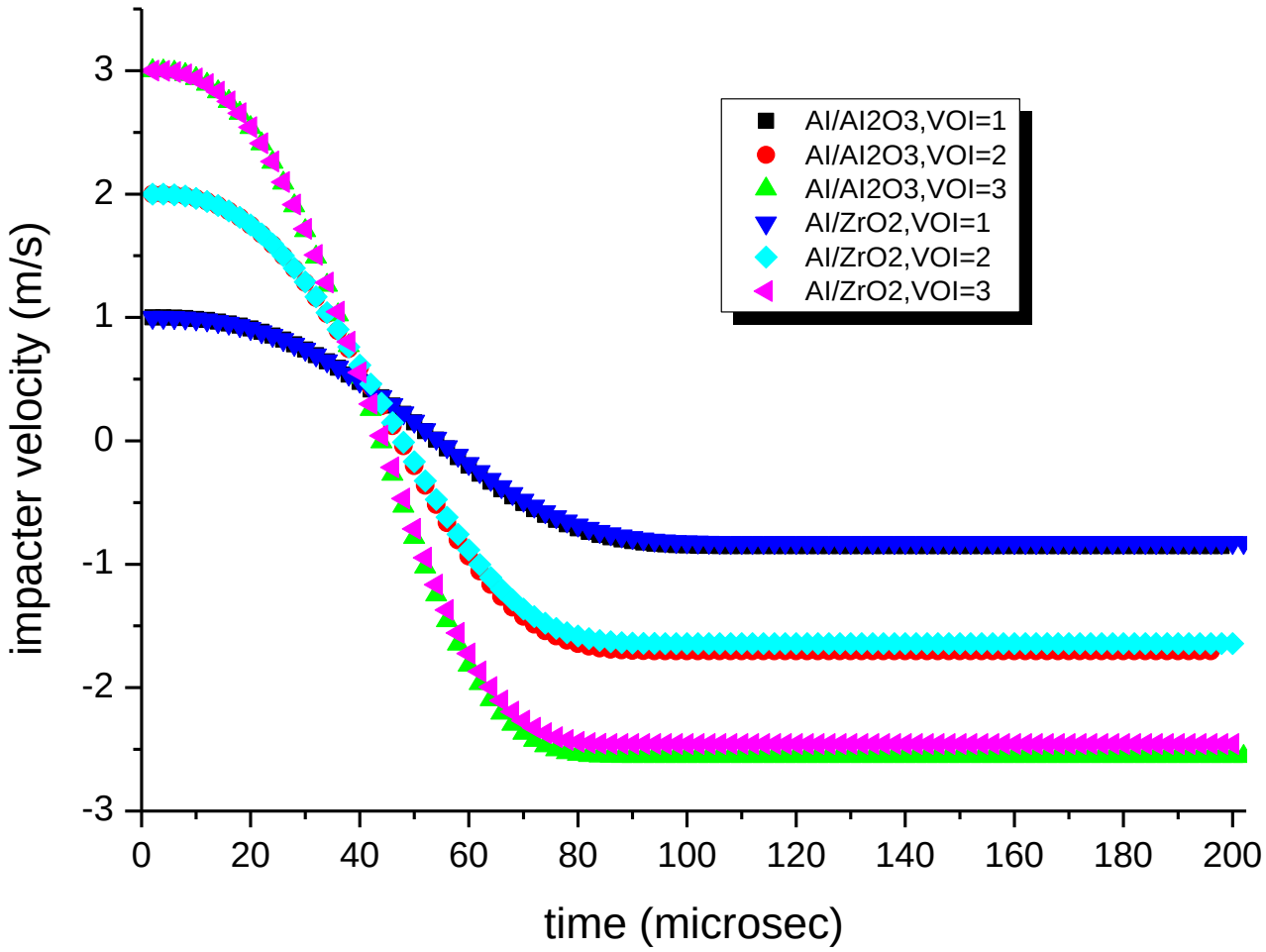

Fig. 13(a) Plot For Impactor Velocity Vs. Time-Step For Power Factor(K) =2

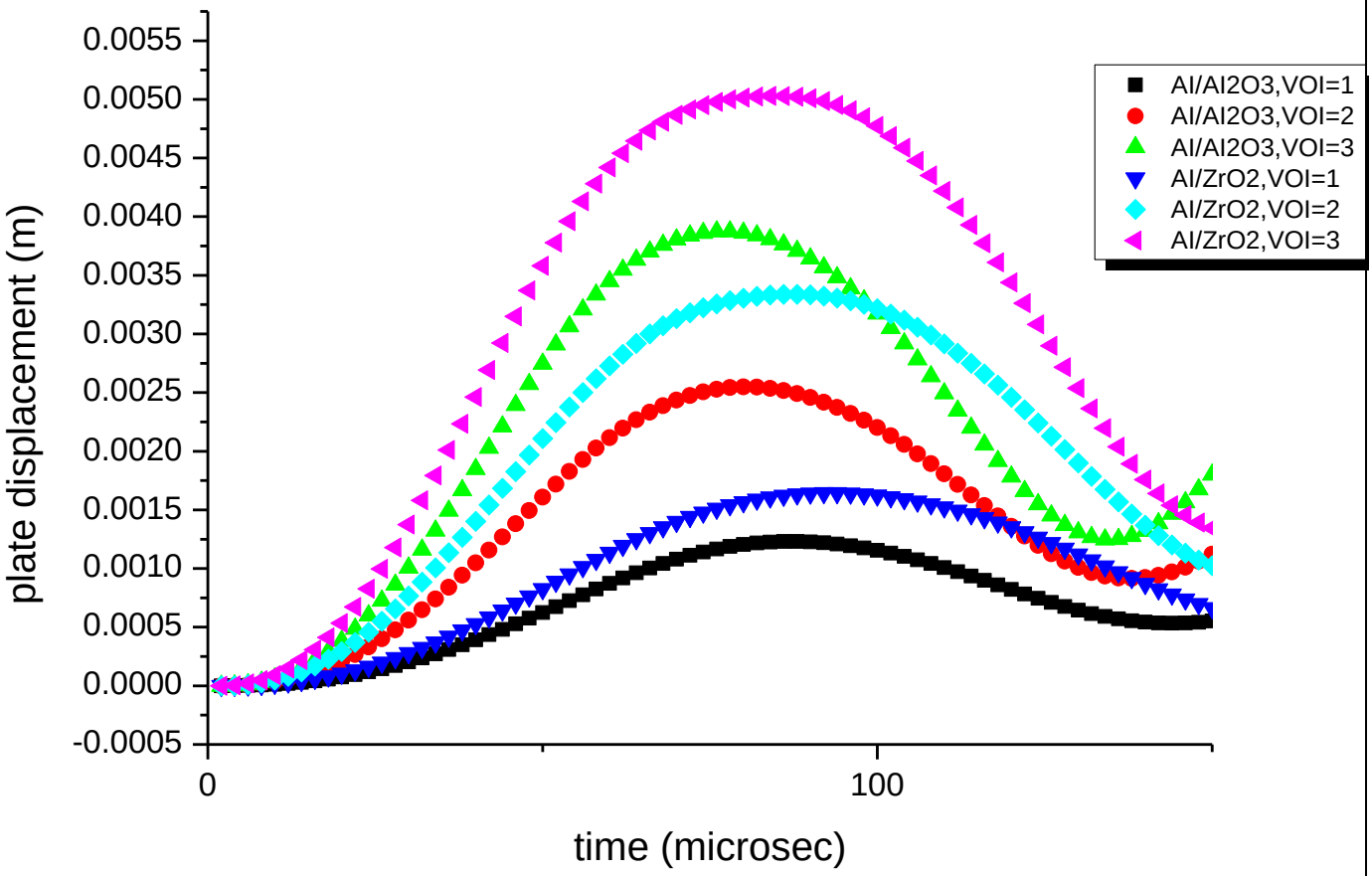

Fig. 13(b) Plot For Plate Displacement Vs time-Step For Power Factor (K)=2

RESULT OF CONTACT FORCE & IMPACTOR DISPLACEMENT FOR (*k*) = 5

The impact behavior (contact force and impactor displacements) of FGM plates for a power index (k) = 5.0 are plotted and presented in **Fig 14(a)** and **14(b)** for Al/Al_2O_3 and Al/ZrO_2 FGM plates for different values of the impactor velocities (VOI). At VOI = 3m/s, For Al/Al_2O_3Maximum value of contact force is 1100N at time-step of 45 μs and its decreases afterwards. For Al/ZrO2 contact force attains maximum value of 1088 N at the time-steps 42 μs and it decrease afterwards. The impactor displacement attains the peak value (0.09 mm) in time-steps of 50 μs for both Al/Al_2O_3 and Al/ZrO2. At VOI=2m/s, For Al/Al_2O_3, the Maximum value of contact force is 682N at time-steps of 46 μs and its decreases afterwards. For Al/ZrO2, the contact force attains maximum value of 670 N at time-steps of 50μs and it decrease afterwards. The impactor displacement is increasing from 0 to the peak value (0.065 mm) in time-steps of 45 μs for $Al/Al_2O_3$and 50μs for Al/ZrO2 and is decreases afterwards. At VOI=1m/s, For Al/Al_2O_3, the contacts force attains maximum value of 297N at time-steps of 50 μs and its decreases afterwards. For Al/ZrO2 contact force attains maximum value of 293 N at the time-steps of 50 μs and it decrease afterwards. The impactor displacement attains the peak value (0.038 mm) in time-steps of 52 μs for both $Al/Al_2O_3$and Al/ZrO2and is decreases afterwards.

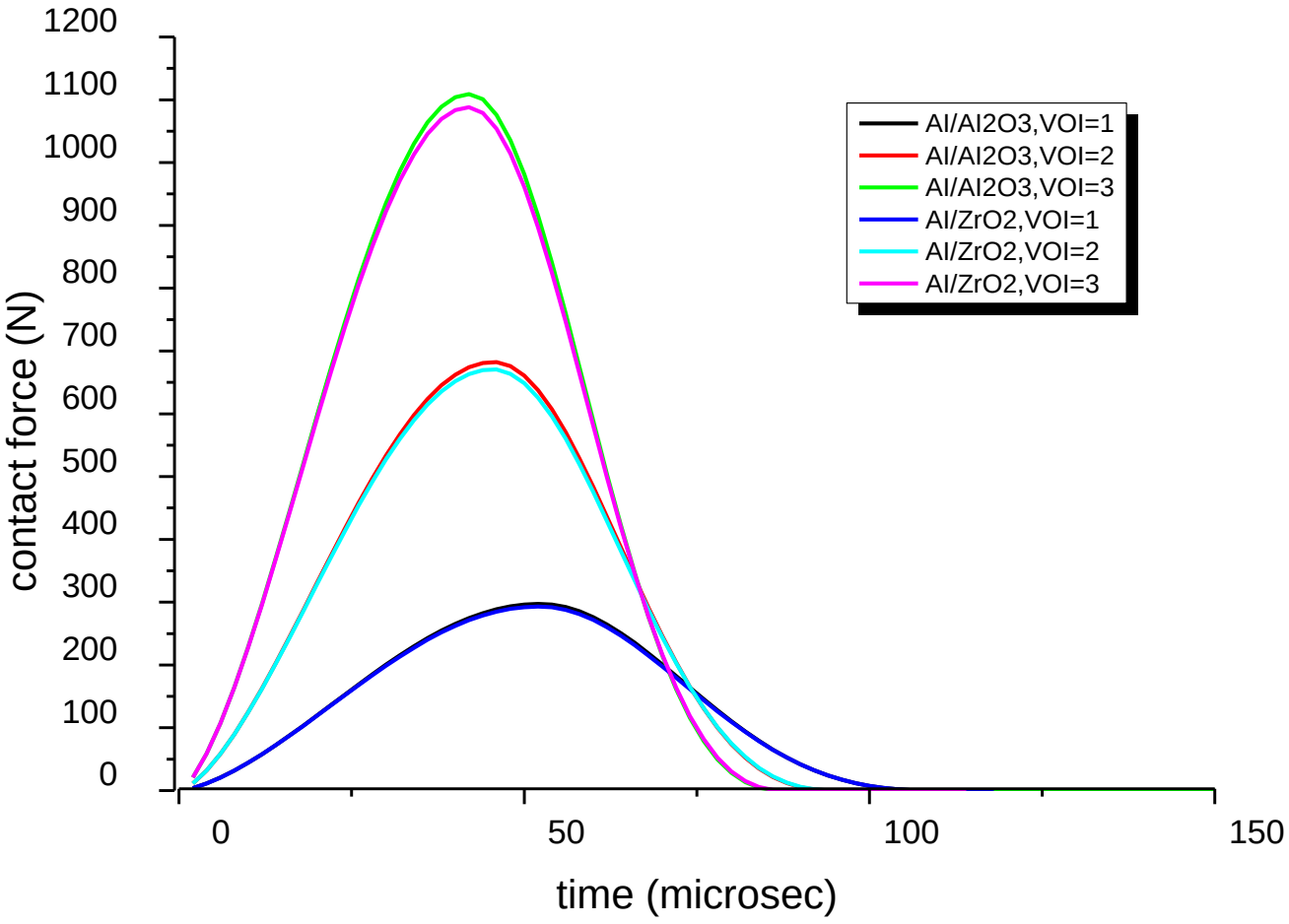

Fig. 14(a) Plot For Contact Force Vs. Time - Step For The Power Factor (K)=5

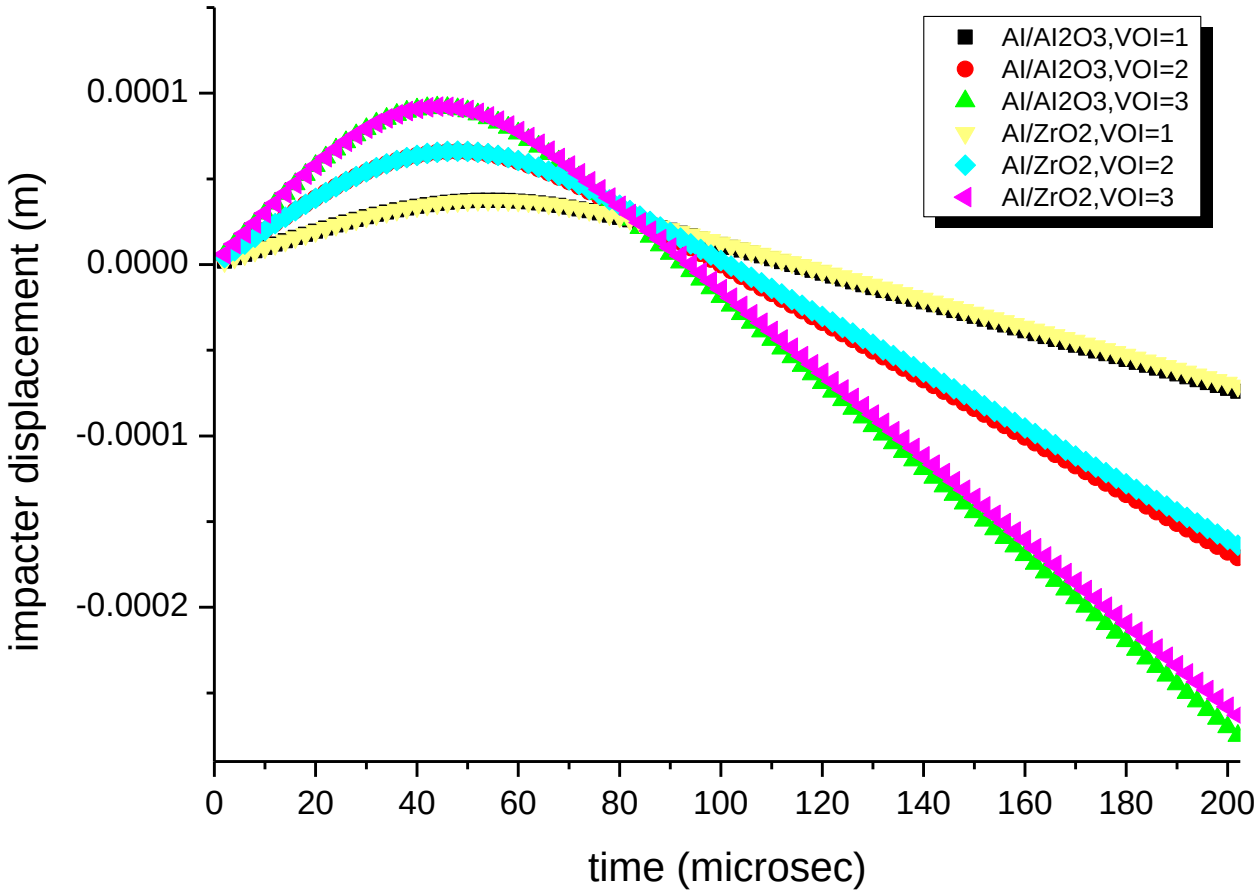

Fig. 14(b) Plot For Impactor Displacement vs. Time-Step For The power Factor (K)=5

RESULT OF IMPACTOR VELOCITY & PLATE DISPLACEMENT FOR (K)= 5

The impact behavior (plate displacement and impactor velocity) of FGM plates for a power index (k) = 5.0 are plotted and presented in **Fig 15(a)** and **15(b)** for Al/Al_2O_3 and Al/ZrO_2 FGM plates for different values of the impactor velocities (VOI). At VOI=3m/s. The impactor velocity for both Al/Al_2O_3& Al/ZrO2 starts from 3 m/s and it decreases sharply to attains value of -2.5m/s for $Al/Al_2O_3$and 2.43 m/s for Al/ZrO2 at time 84 µs. and 42 µs. Plate displacement for Al/Al_2O_3attains first maxima of 4.4 mm at time-step of 80 µs then further rises to second maxima of 5.6mm at time 210 µs. For Al/ZrO2 attains first maxima of 5.2 mm at 90 µs then further rises to a maximum of 6.8 mm at time of 240 µs. At VOI=2m/s, the impactor velocity for both Al/Al_2O_3& Al/ZrO2 starts from 2m/s and it decreases sharply to attains value of -1.65m/s for both Al/Al2O3and Al/ZrO2 at time 90 µs. Plate displacement for Al/Al_2O_3attains first maxima of 2.9 mm at time-step of 84 µs then further rises to second maxima of 3.6 mm at time 214 µs. For Al/ZrO2 attains first maxima of 3.5mm at 90 µs then further rises to second maxima of 4.5 mm at time of 240 µs. At VOI=1m/s, the impactor velocity for both Al/Al_2O_3& Al/ZrO2

starts from 1 m/s and it decreases sharply to attains value of -0.83m/s for both $Al/Al_2O_3$and Al/ZrO2 at time 104 µs. Plate displacement for Al/Al_2O_3attains first maxima of 1.4mm at time-step of 84 µs then further rises to second maxima of 1.7mm at time 110 µs. For Al/ZrO2 attains first maxima of 1.7 mm at 100 µs then further rises to second maxima of 2.2 mm at time of 250 µs.

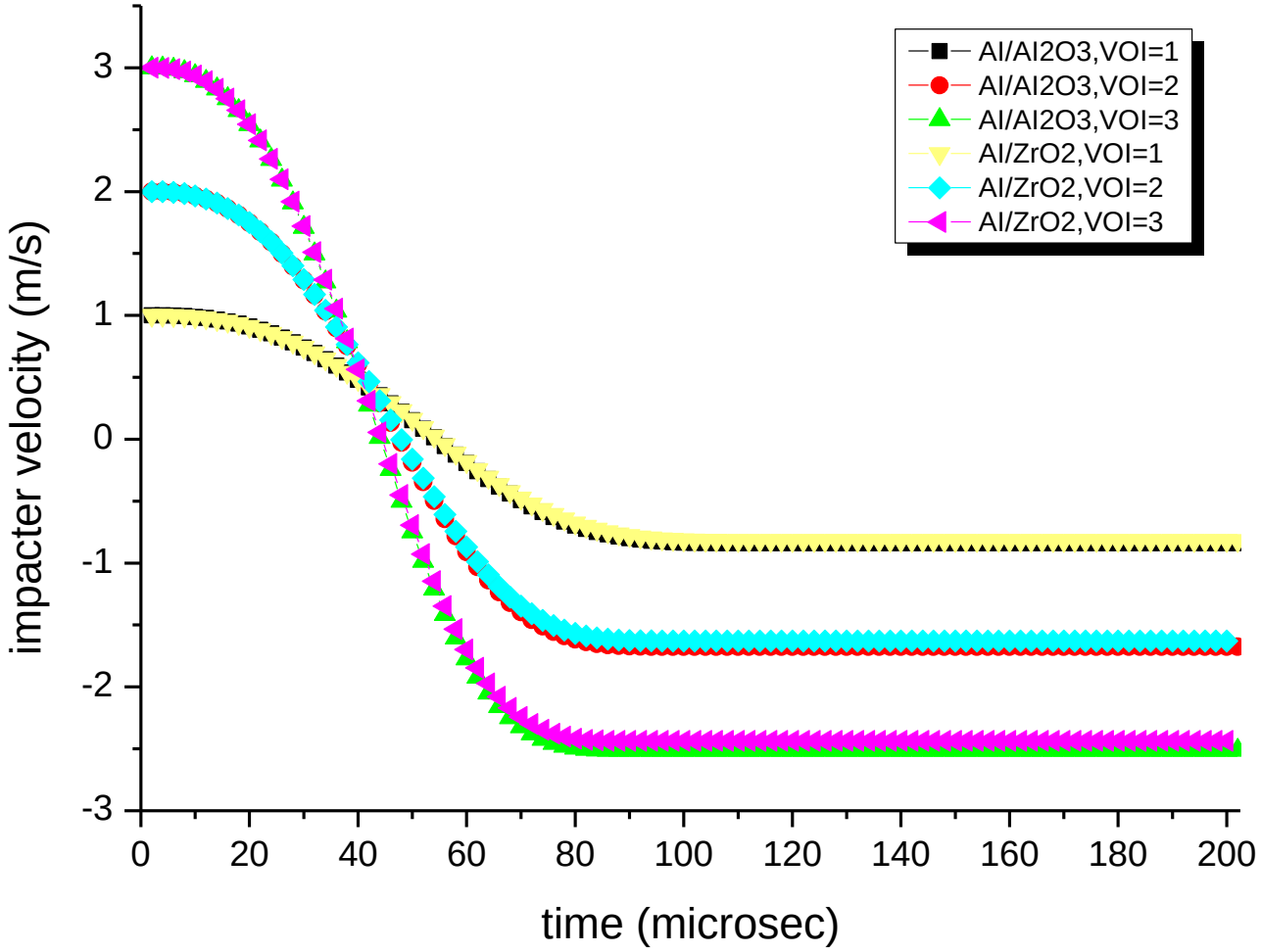

Fig 15(a) Plot For Impactor Velocity Vs. Time-Step For Power Factor(K) =5

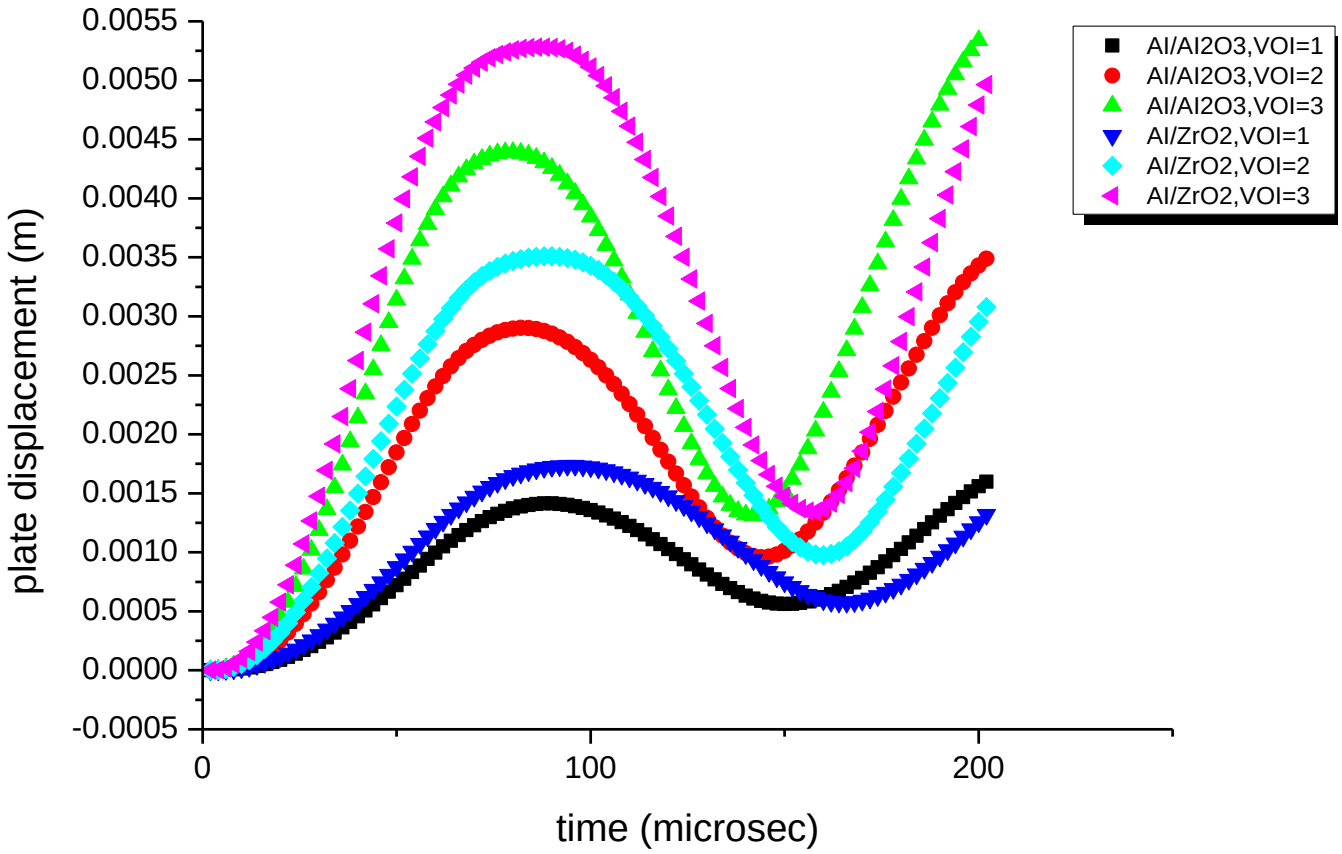

Fig 15(b) Plot For Plate Displacement Vs time-Step For Power Factor (*k*)=5

RESULT OF CONTACT FORCE & IMPACTOR DISPLACEMENT FOR (*k*)= 10

The impact behavior (Contact force and impactor displacement) of FGM plates for a power index (*k*) = 10.0 are plotted and presented in **Fig 16(a)** and **16(b)** for Al/Al_2O_3 and Al/ZrO_2 FGM plates for different values of the impactor velocities (VOI). At VOI=3m/s. At VOI=3m/s, For Al/Al_2O_3, The Maximum value of contact force is 1100N at time-step of 42 µs and its decreases afterwards. For Al/ZrO2 contact force attains maximum value of 1083 N at the time-steps 42 µs and it decrease afterwards. The impactor displacement attains the peak value (0.092 mm) in time-steps of 50 µs for both Al/Al_2O_3andAl/ZrO2. At VOI= 2m/s, For Al/Al_2O_3, The Maximum value of contact force is 677N at time-steps of 50 µs and its decreases afterwards. For Al/ZrO2 contact force attains maximum value of 667 N at time-steps of 92 µs and it decrease afterwards. The impactor displacement is increasing from 0 to the peak value (0.066 mm) in time-steps of 50 µs for both $Al/Al_2O_3$and Al/ZrO2 and is decreases afterwards. At VOI=1m/s, For Al/Al_2O_3, the contacts force attains maximum value of 295N at time-steps of 52 µs and its decreases afterwards. For Al/ZrO2contact force attains maximum value of 292N at the time-steps of 52 µs and it decrease afterwards. The impactor displacement attains the peak value (0.03 mm) in time-steps of 55 µs for both $Al/Al_2O_3$and Al/ZrO2and is decreases afterwards.

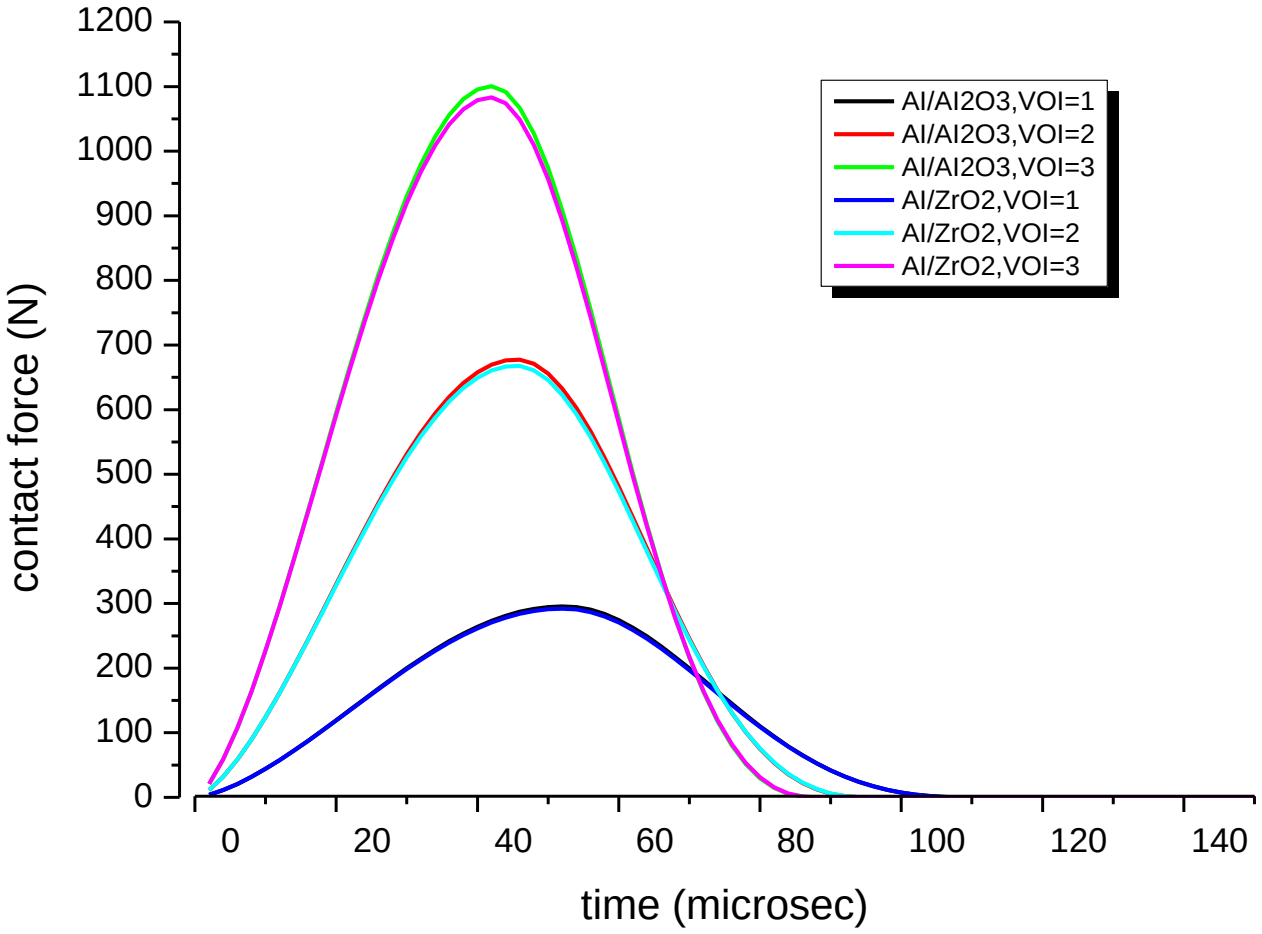

Fig. 16(a) Plot For Contact Force Vs. Time -Step For The Power Factor (K) =10

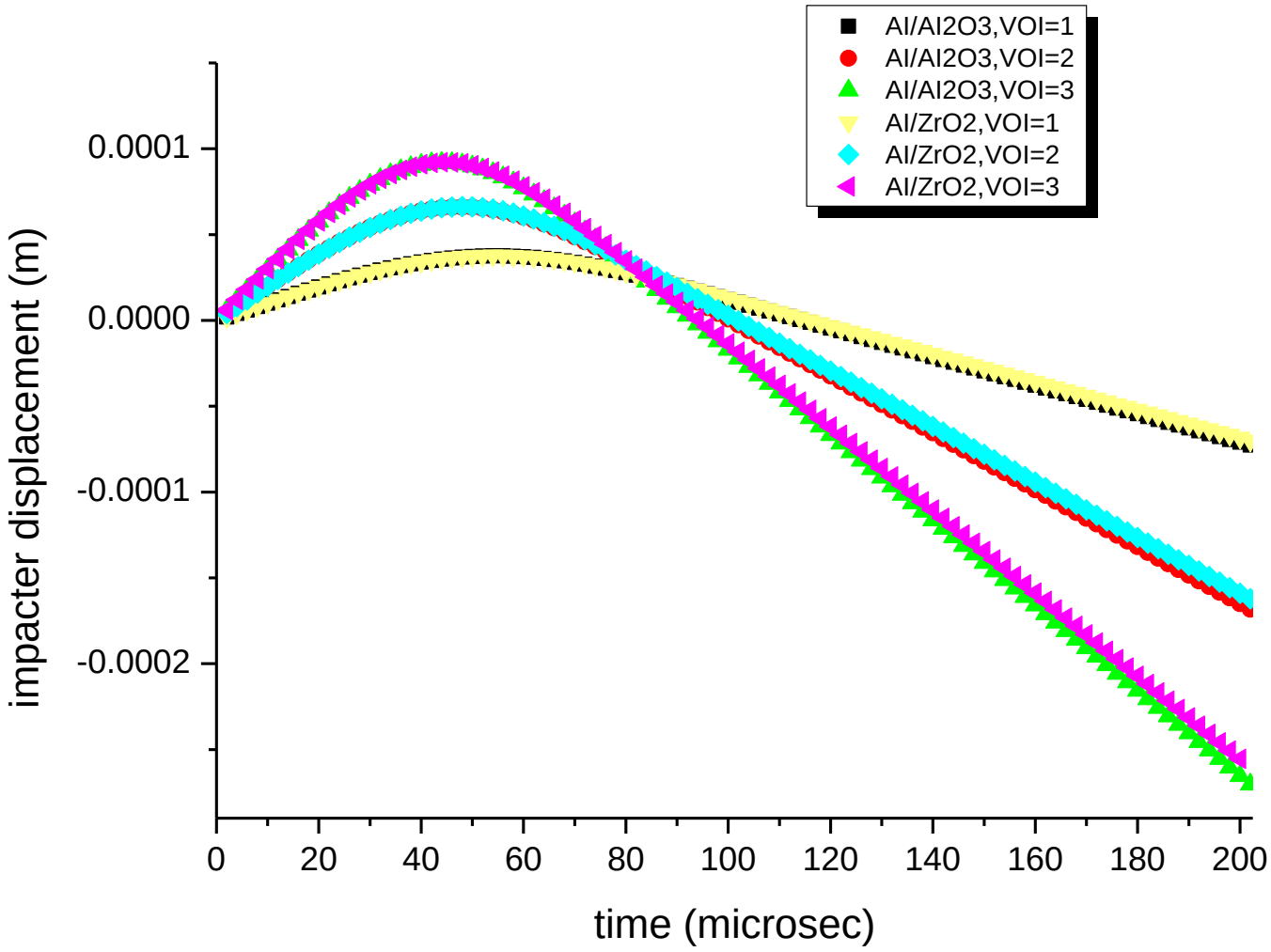

Fig. 16(b) Plot For Impactor Displacement vs. Time-Step For The Power Factor (K)=10

RESULT OF IMPACTOR VELOCITY & PLATE DISPLACEMENT FOR (*k*) = 10

The impact behavior (Plate displacement and impactor velocity) of FGM plates for a power index (*k*) = 10.0 are plotted and presented in **Fig 17(a)** and **17(b)** for Al/Al_2O_3 and Al/ZrO_2 FGM plates for different values of the impactor velocities (VOI). At VOI=3m/s, the impactor velocity for both Al/Al_2O_3& Al/ZrO2 starts from 3 m/s and it decreases sharply to attains value of -2.75m/s for both $Al/Al_2O_3$and Al/ZrO2 at time 80 µs. Plate displacement for Al/Al_2O_3attains first maxima of 4.5mm at time-step of 50 µs then further rises to second maxima of 6.5mm at time 200 µs. For Al/ZrO2 attains first maxima of 5.5mm at 100 µs then to a lower dip at 150 microseconds and further rises to a maximum of 7.5mm at time of 250 µs. At VOI=2m/s, the impactor velocity for both Al/Al_2O_3& Al/ZrO2 starts from 2m/s and it decreases sharply to attains value of -1.65m/s for both Al/Al2O3and Al/ZrO2 at time 85 µs. Plate displacement for Al/Al_2O_3attains first maxima of 3mm at time-step of 80µs then further rises to second maxima of 3.5mm at time 150 µs. For Al/ZrO2 attains first maxima of 3.5mm at 100 µs then further rises to second maxima of 5 mm at time of 250 µs. At VOI=1m/s, the impactor velocity for both Al/Al_2O_3 and Al/ZrO2 starts from 1 m/s and it decreases sharply to attains value of -0.81m/s for both

$Al/Al_2O_3$and Al/ZrO2 at time 100 μs. Plate displacement for Al/Al_2O_3attains first maxima of 1.5mm at time-step of 50 μs then further rises to second maxima of 1.9 mm at time 114 μs. For Al/ZrO2 attains first maxima of 1.8mm at 94 μs then further rises to second maxima of 2.29 mm at time of 252 μs.

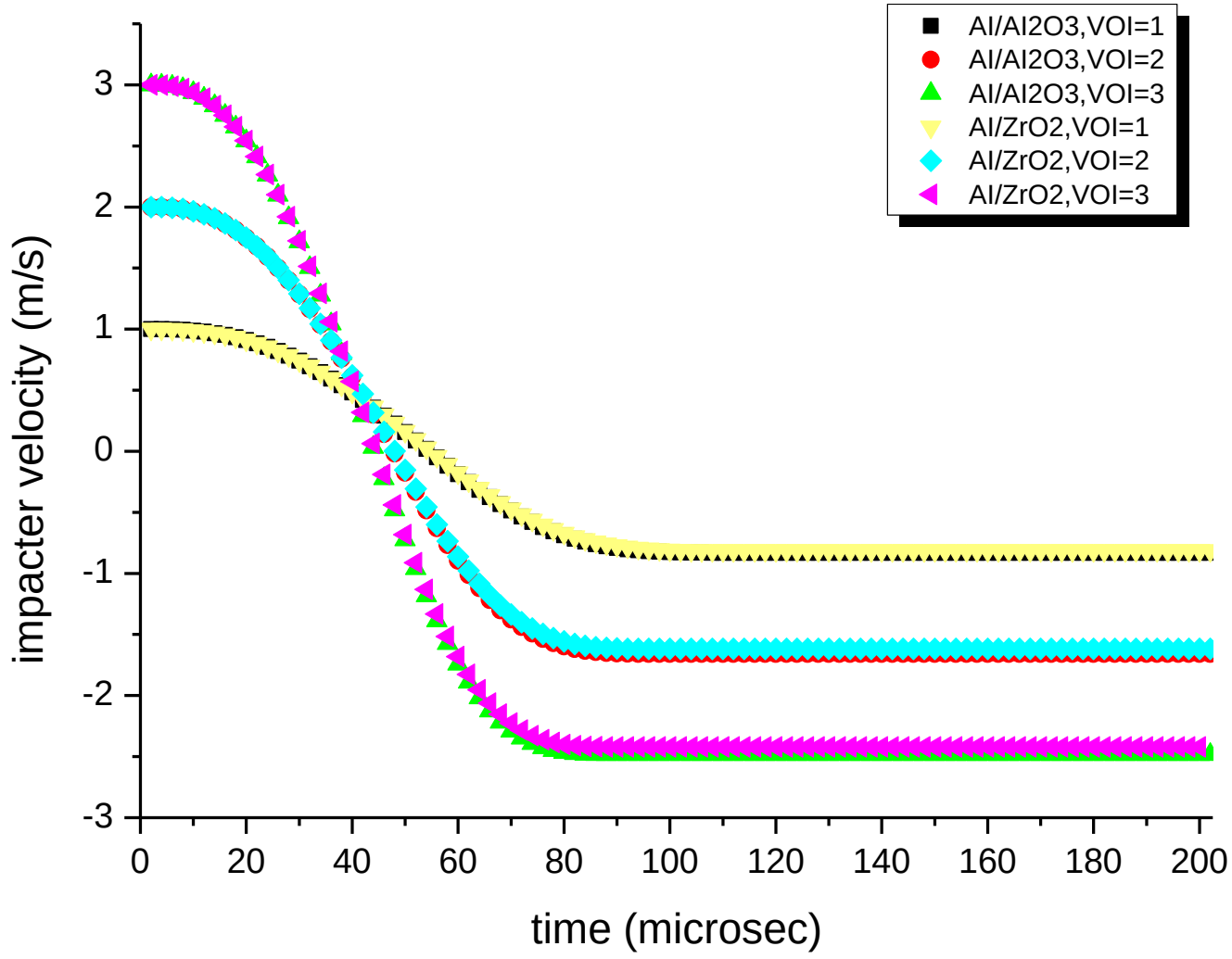

Fig. 17(a) Plot of Impactor Velocity Vs. Time-Step for Power Factor (K) =10

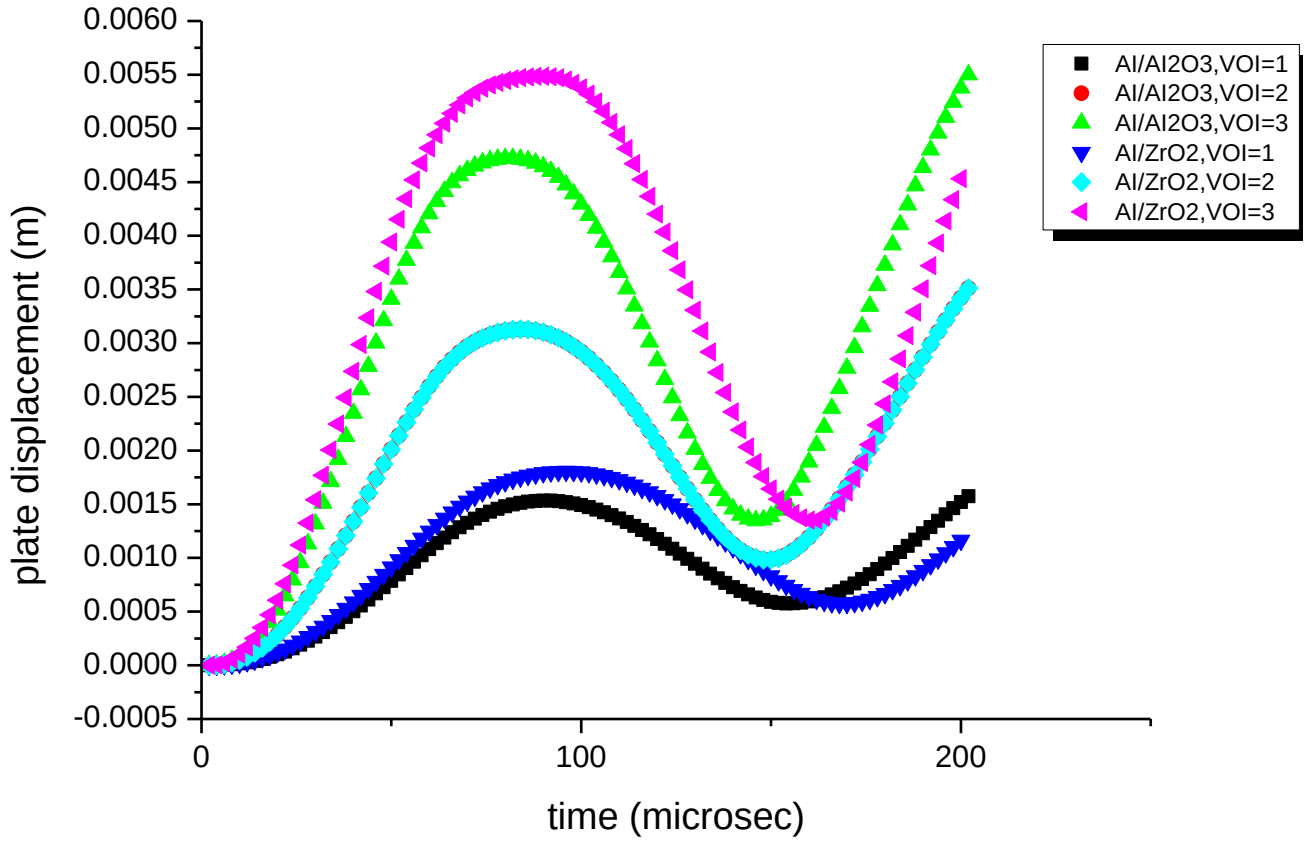

Fig. 17(b) Plot of Plate Displacement Vs Time-Step for Power Factor (K)=10

The impact behavior (Contact Force and Plate Displacement) of FGM plates for a power index (k)=0.0 are plotted and presented in **Fig 18** for Al/Al_2O_3 and $SUS304/Si_3N_4$ FGM plates for different values of the impactor velocities (VOI). At VOI=3m/s, For Al/Al_2O_3, The Maximum value of contact force is 1158N at time-step of 50 µs and its decreases afterwards. For SUS3O4/Si3O4contact force attains maximum value of 1145 N at the time-steps 42 µs and it decrease afterwards. At VOI=2m/s, For Al/Al_2O_3, The Maximum value of contact force is 710N at time-steps of 52 µs and its decreases afterwards. For SUS3O4/Si3O4 contact force attains maximum value of 699 N time-steps of 50µs and it decrease afterwards. At VOI=1m/s, For Al/Al_2O_3contacts force attains maximum value of 307N at time-steps of 54 µs and its decreases afterwards. For SUS3O4/Si3O4 contact force attains maximum value of 308 N at the time-steps of 56 µs and it decrease afterwards. Plate displacement for attains first maxima of 2mm at time-step of 74 µs then further rises to second maxima of 2.67mm at time 164 µs. For SUS3O4/Si3O4 attains first maxima of 3mm at 80 µs then further rises to a maximum of 4.1 mm at time of 206 µs. At VOI=2m/s, Plate displacement for Al/Al2O3 attains first maxima of 1.3 mm at time-step of 80 µs then further rises to second maxima of 1.74 mm at time 164 µs. For SUS3O4/Si3O4 attains first maxima of 2.5mm at 80 µs then further rises to second maxima of 3.2 mm at time of 200 µs. At VOI=1m/s, Plate displacement for Al/Al_2O_3 attains first maxima of .6mm at time-step of 80 µs then further rises to second maxima of 0.84mm at time 168 µs. For SUS3O4/Si3O4 attains first maxima of 1mm at 100 µs then further rises to second maxima of 1.5 mm at time of 200 µs

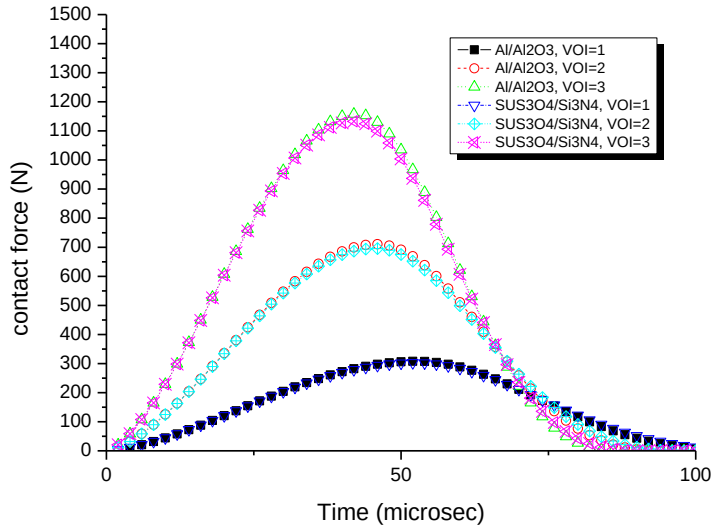

(a)

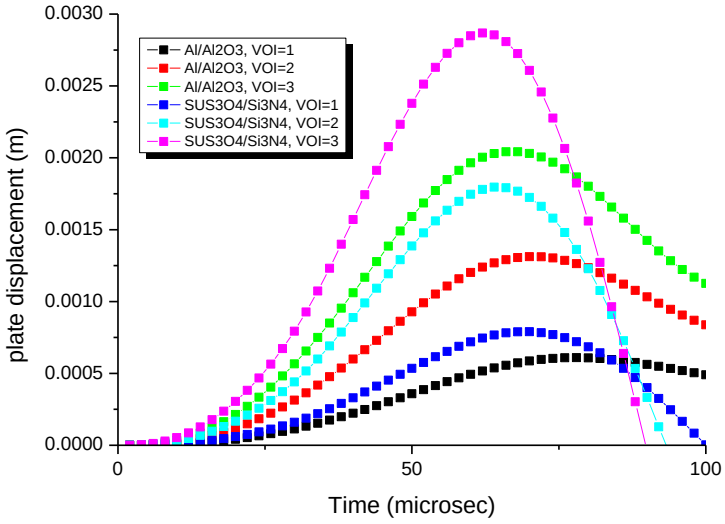

(b)

Fig. 18 Plot of Contact Force and Plate Displacement Vs. Time -Step for The Power Factor (K) =0

The impact behavior (Contact Force and Plate Displacement) of FGM plates for a power index (k)=2.0 are plotted and presented in **Fig 19** for Al/Al_2O_3 and $SUS304/Si_3N_4$ FGM plates for different values of the impactor velocities (VOI). At VOI=3m/s, for Al/Al2O3, the maximum value of contact force is 1100N at a time-step of 45 µs and then decreases afterwards. For SUS3O4/Si3O4 contact force attains maximum value of 1150 N at the time-steps 50 µs and it decrease afterwards. At VOI=2m/s, For Al/Al_2O_3, the Maximum value of contact force is 650N at time-steps of 50 µs and its decreases afterwards. For SUS3O4/Si3O4 contact force attains

maximum value of 675 N at time-steps of 45μs and it decrease afterwards. At VOI=1m/s, For Al/Al_2O_3, the contacts force attains maximum value of 299N at time-steps of 50 μs and its decreases afterwards. For SUS3O4/Si3O4 contact force attains maximum value of 294 N at the time-steps of 50 μs and it decrease afterwards. At VOI=3m/s, Plate displacement for Al/Al_2O_3attains first maxima of 3.8 mm at time-step of 80 μs then further rises to second maxima of 4.9 mm at time 200 μs. For SUS3O4/Si3O4 attains first maxima of 3mm at 100 μs then to a lower dip at 150 microseconds and further rises to a maximum of 5mm at time of 250 μs. At VOI=2m/s, Plate displacement for Al/Al_2O_3attains first maxima of 2.5mm at time-step of 80μs then further rises to second maxima of 3mm at time 200 μs. For SUS3O4/Si3O4 attains first maxima of 2.1mm at 80 μs then further rises to second maxima of 3.7 mm at time of 250 μs. At VOI=1m/s, Plate displacement for Al/Al_2O_3attains first maxima of 1.2 mm at time-step of 84 μs then further rises to second maxima of 1.5 mm at time 210 μs. For SUS3O4/Si3O4 attains first maxima of 1.4mm at 100 μs then further rises to second maxima of 2 mm at time of 200 μs.

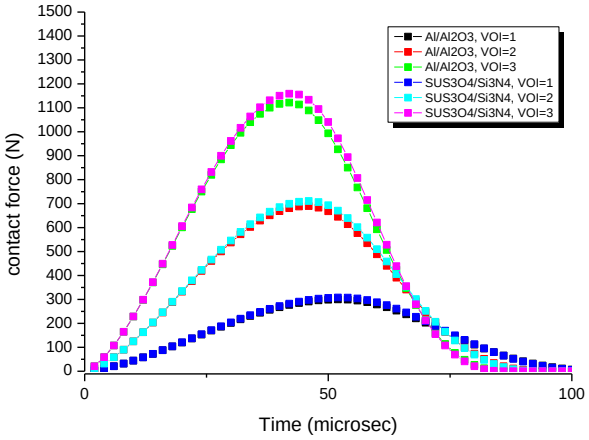

(a)

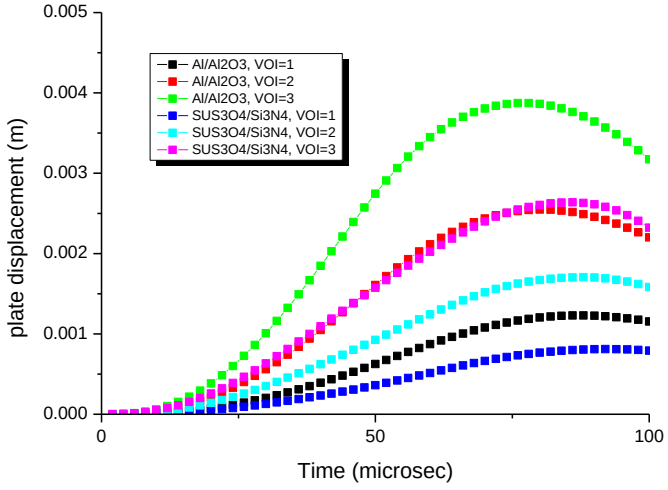

(b)

Fig. 19 PLOT OF CONTACT FORCE Vs. TIME -STEP FOR THE POWER FACTOR (K) = 2

The impact behavior (Contact Force and Plate Displacement) of FGM plates for a power index (k)=5.0 are plotted and presented in **Fig 20** for Al/Al_2O_3 and $SUS304/Si_3N_4$ FGM plates for different values of the impactor velocities (VOI). At VOI = 3m/s, For Al/Al_2O_3Maximum value of contact force is 1100N at time-step of 45 μs and its decreases afterwards. For SUS3O4/Si3O4 contact force attains maximum value of 1159 N at the time-steps 42 μs and it decrease afterwards. At VOI=2m/s, For Al/Al_2O_3, the Maximum value of contact force is 682N at time-steps of 46 μs and its decreases afterwards. For SUS3O4/Si3O4, the contact force attains maximum value of 670 N at time-steps of 50μs and it decrease afterwards. At VOI=1m/s, For Al/Al_2O_3, the contacts force attains maximum value of 297N at time-steps of 50 μs and its decreases afterwards. For SUS3O4/Si3O4 contact force attains maximum value of 308 N at the time-steps of 50 μs and it decrease afterwards. At VOI=3m/s, Plate displacement for Al/Al_2O_3attains first maxima of 4.4 mm at time-step of 80 μs then further rises to second maxima of 5.6mm at time 210 μs. For SUS3O4/Si3O4 attains first maxima of 2.5 mm at 90 μs then further rises to a maximum of 3.8 mm at time of 240 μs. At VOI=2m/s, Plate displacement for Al/Al_2O_3attains first maxima of 2.9 mm at time-step of 84 μs then further rises to second maxima of 3.6 mm at time 214 μs. For SUS3O4/Si3O4 attains first maxima of 2mm at 90 μs then further rises to second maxima of 3.5 mm at time of 240 μs. At VOI=1m/s, Plate displacement for Al/Al_2O_3attains first maxima of 1.4mm at time-step of 84 μs then further rises to second maxima of 1.7mm at time 110 μs. For SUS3O4/Si3O4 attains first maxima of .9 mm at 100 μs then further rises to second maxima of 2.2 mm at time of 250 μs.

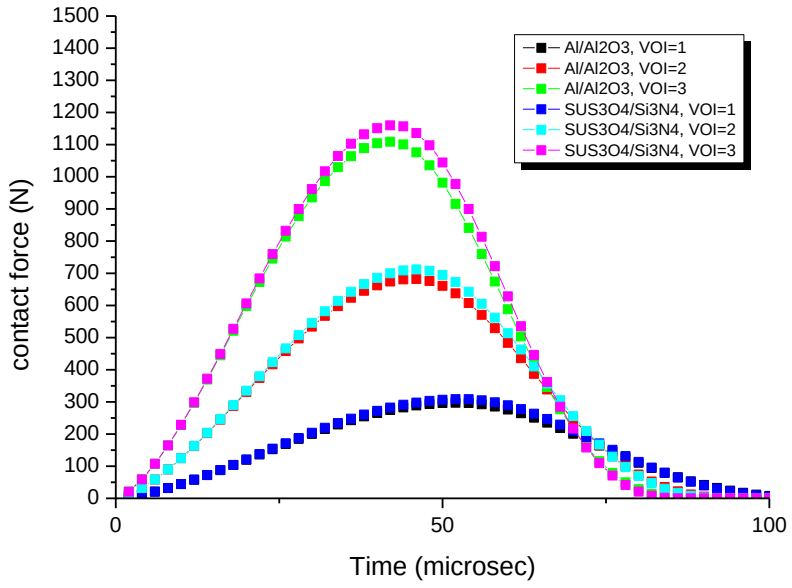

(a)

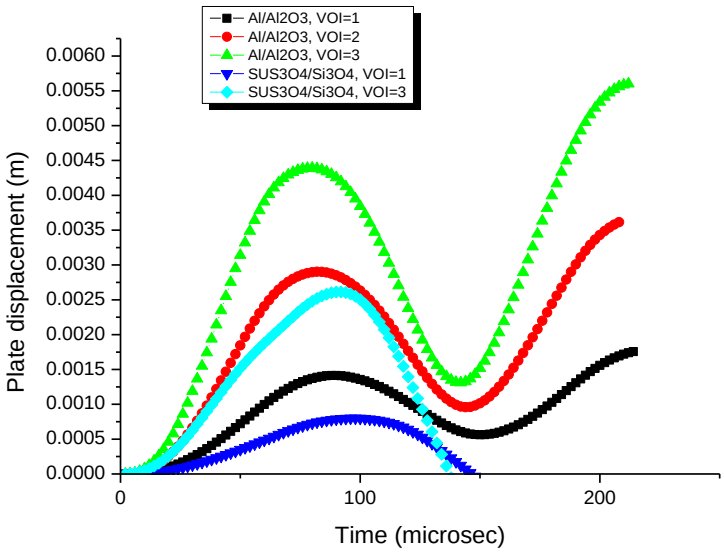

(b)

Fig. 20 PLOT FOR CONTACT FORCE Vs. TIME -STEP FOR THE POWER FACTOR (K) = 5

The impact behavior (Contact Force and Plate Displacement) of FGM plates for a power index (k)=10.0 are plotted and presented in **Fig 21** for Al/Al2O3 and SUS304/Si3N4 FGM plates for different values of the impactor velocities (VOI). FOR VOI=3 m/s. At VOI=3m/s, For Al/Al2O3, The Maximum value of contact force is 1100N at time-step of 42 µs and its decreases afterwards. For SUS3O4/Si3O4 contact force attains maximum value of 1159 N at the time-steps 42 µs and it decrease afterwards. At VOI= 2m/s, For Al/Al_2O_3, The Maximum value of contact force is 677N at time-steps of 50 µs and its decreases afterwards. For SUS3O4/Si3O4 contact force attains maximum value of 711 N at time-steps of 92 µs and it decrease afterwards. At VOI=1m/s, For Al/Al_2O_3, the contacts force attains maximum value of 295N at time-steps of 52 µs and its decreases afterwards. For SUS3O4/Si3O4 contact force attains maximum value of 308N at the time-steps of 52 µs and it decrease afterwards. At VOI=3m/s, Plate displacement for Al/Al_2O_3attains first maxima of 4.5mm at time-step of 50 µs then further rises to second maxima of 6.5mm at time 200 µs. For SUS3O4/Si3O4 attains first maxima of 2.6mm at 100 µs then to a lower dip at 150 microseconds and further rises to a maximum of 2.85mm at time of 250 µs. At VOI=2m/s, Plate displacement for Al/Al_2O_3attains first maxima of 3mm at time-step of 80µs then further rises to second maxima of 3.5mm at time 150 µs. For SUS3O4/Si3O4 attains first maxima of 1.7mm at 100 µs then further rises to second maxima of 1.72 mm at time of 250 µs. At VOI=1m/s, Plate displacement for Al/Al_2O_3attains first maxima of 1.5mm at time-step of 50 µs then further rises to second maxima of 1.9 mm at time 114 µs. For SUS3O4/Si3O4 attains first maxima of 0.8mm at 94 µs then further rises to second maxima of 0.9 mm at time of 252 µs.

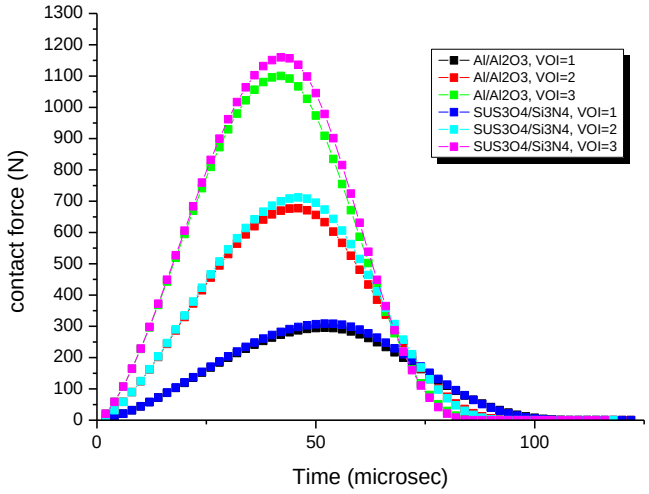

(a)

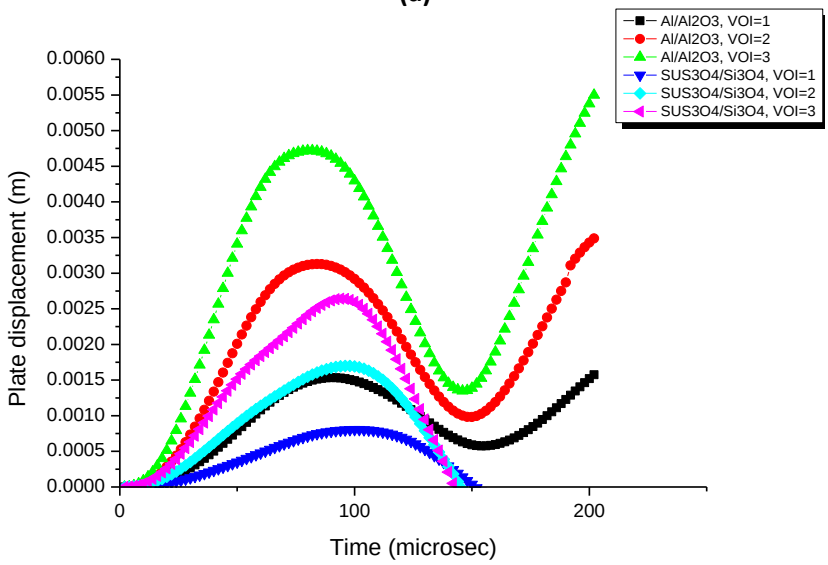

(b)

Fig. 21 PLOT OF CONTACT FORCE Vs. TIME -STEP FOR THE POWER FACTOR (K) =10

CONCLUSIONS

- An increase in the Contact Force, plate deflection and impactor deflection is observed with an increase in the impact velocity.
- The FGM Al/Al2O3displays higher values of the contact force compared to the FGM Al/ZrO2. However, for lower impactor velocities (i.e. VOI= 1m/s), both $Al/Al_2O_3$and Al/ZrO2 gives similar result.
- The FGM Al/ZrO2 displays higher values of the plate displacement compared to the FGM $Al/Al_2O_3$and with increase in the value of velocity of impact this difference in the value seems to rise.
- Difference in the value of power factor doesn`t cause in any major difference in value of contact force, plate displacement, and impactor deflection.
- The velocity of impacts doesn`t show exact replication in the negative axis (i.e. if VOI=3m/s then in negative axis it goes to -2.75 m/s only) which shows there is a loss of energy.
- The plate deflection was significant as compared to impactor deflections irrespective of velocity of impact and power factor.

REFERENCES

[1] N.Noda, Thermal stresses in functionally graded materials, Journal of Thermal Stresses 22(1999)477–512

[2] M.H. Yas, M. Shakeri, M. Heshmati, S. Mohammadi Layer-wise finite element analysis of functionally graded cylindrical shell under dynamic load J. Mech. Sci. Technol., 25 (3) (2011), pp. 597-604

[3] D. Lin, Q. Li, W. Li, M. SwainBone remodeling induced by dental implants of functionally graded materials J. Biomed. Mater.Res. Part B Appl. Biomater. Off. J. Soc. Biomater. Japanese Soc. Biomater.Australian Soc. Biomater. Korean Soc. Biomater., 92 (2) (2010), pp. 430-438

[4] Wagner, Ronald. (2020). ABAQUS Tutorial: How to model graded material (GM) and functionally graded material (FGM) In ABAQUS CAE.

[5] A.H.A. Hassan, İ. Keleş FGM Modelling using Dummy Thermal Loads J. Selcuk Int. Sci. Technol., 1 (10–16) (2017)

[6] S.J. Singh, S.P. Harsha Nonlinear dynamic analysis of sandwich S-FGM plate resting on pasternak foundation under thermal environment Eur. J. Mech. A/Solids, 76 (2019), pp. 155-179

[7] N. Grover, B.N. Singh, D.K. Maiti New nonpolynomial shear-deformation theories for structural behavior of laminated-composite and sandwich plates AIAA J., 51 (8) (2013), pp. 1861-1871, 10.2514/1.J052399

[8] A. Gupta, V. Krishna, V. Boddu, P. Vemulapalli, N. Unnava, B.N. Agrawal Geometric/microstructural imperfection sensitivity in the vibration characteristics of geometrically non-uniform functionally graded plates with mixed boundary condition Mech. Based Des. Struct. Mach. (2021), pp. 1-35, 10.1080/15397734.2021.1886947

[9] S. Merdaci, H.M. Adda, B. Hakima, R. Dimitri, F. Tornabene Higher-Order Free Vibration Analysis of Porous Functionally Graded Plates J. Compos. Sci., 5 (11) (2021), p. 305, 10.3390/jcs5110305

[10] Garg A., Mohamed-OuejdiBelarbi H.D., Chakrabarti A. A review of the analysis of sandwich FGM structures Compos. Struct., 258 (2021), Article 113427

[11] Tetougueni C.D., Maiorana E., Zampieri P., Pellegrino C. Plate girders behavior under in-plane loading: A review Eng. Fail. Anal., 95 (2019), pp. 332-358

[12] J. Reddy, Z.Q. Cheng Three-dimensional thermomechanical deformations of functionally graded rectangular plates Eur J Mech A/Solids, 20 (2001), pp. 841-855

[13] Y.Z. Wang, D. Liu, Q. Wang, J.Z. Zhou Asymptotic analysis of thermoelastic response in functionally graded thin plate subjected to a transient thermal shock Compos Struct, 139 (2016), pp. 233-242

[14] M.B. Yihunie, E.W. Dereje, T.C. Ewnetu, A.A. Solomon, K.S. Senthil, P. Velmurugan. Effect of volumetric fraction index on temperature distribution in thick-walled functionally

graded material made cylinder. Mater.Today Proc. 2021. https://doi.org/10.1016/j.matpr.2021.01.042.
[15] M.A. Xavior, D. Nishanth, N. Navin Kumar, P. Jeyapandiarajan Synthesis and Testing of FGM made of ABS Plastic Material Mater. Today Proc., 22–4 (2020), pp. 1838-1844.
16. Kiani, Y., Sadighi, M., Salami, S.J. and Eslami, M.R., 2013. Low velocity impact response of thick FGM beams with general boundary conditions in thermal field. *Composite Structures*, *104*, pp.293-303.
17. Jam, J.E. and Kiani, Y., 2015. Low velocity impact response of functionally graded carbon nanotube reinforced composite beams in thermal environment. *Composite Structures*, *132*, pp.35-43.
18. Mirzaei, M. and Kiani, Y., 2016. Free vibration of functionally graded carbon nanotube reinforced composite cylindrical panels. *Composite Structures*, *142*, pp.45-56.
19. Mao, Y.Q., Fu, Y.M., Chen, C.P. and Li, Y.L., 2011. Nonlinear dynamic response for functionally graded shallow spherical shell under low velocity impact in thermal environment. *Applied Mathematical Modelling*, *35*(6), pp.2887-2900.
20.Eghtesad, A., Shafiei, A.R. and Mahzoon, M., 2012. Study of dynamic behavior of ceramic–metal FGM under high velocity impact conditions using CSPM method. Applied Mathematical Modelling, 36(6), pp.2724-2738.
[21] Qatu MS, Leissa AW. Vibration studies for laminated composite twisted cantilever plates. Int J MechSci 1991;33(11):927–40.
[22] Liew KM, Lim CM, Ong LS. Vibration of pretwisted cantilever shallow conical shells. Int J Solids Struct 1994; 31:2463–74.
[23] Mcgee OG, Chu HR. Three-dimensional vibration analysis of rotating laminated composite blades. J Eng Gas Turbines Power Trans ASME 1994; 116:663–71.
[24] Lee JJ, Yeom CH, Lee I. Vibration analysis of twisted cantilever conical composite shells. J Sound Vib 2002;255(5):965–82.
[25] Shen MHH, Grady JE. Free vibrations of delaminated beams. J AIAA 1992; 30(5):1361–70.
[26] Krawczuk M, Ostachowicz W, Zak A. Dynamics of cracked composite material structures. J ComputMech 1997;20:79–83.
[27] Tracy JJ, Pardoen GC. Effect of delamination on the natural frequencies of composite laminates. J Compos Mater 1989;23:1200–15.
[28] Paolozzi A, Peroni I. Detection of debonding damage in a composite plate through natural frequency variations. J ReinfPlast Compos 1992;9:369–89.
[29] Tenek LH, Hennekell EG, Gunzburger MD. Vibration of delaminated composite plates and some applications to non-destructive testing. Compos Structure 1993;23:253–62.
[20] Karmakar A, Kishimoto K. Free vibration analysis of delaminated composite pretwisted rotating shells – a finite element approach. JSME Int J Ser A 2006; 49(4):492–502.
[31] Whitney JM, Ashton JE. Effect of environment on the elastic response of layered composite plates. J AIAA 1971;9:1708–13.

[32] Dhanaraj RD, Palaninathan. Free vibrational characteristics of composite laminates under initial stress. In: Proceedings of the seminar on science and technology of composites, adhesives and sealants. Bangalore, India; 1989.p. 245–51.
[33] Sai Ram KS, Sinha PK. Hygrothermal effects on the free vibration of laminated composite plates. J Sound Vib 1992;158(1):133–48.
[34] Parhi PK, Bhattacharyya SK, Sinha PK. Hygrothermal effects on the dynamic behavior of multiple delaminated composite plates and shells. J Sound Vibration 2001;248(2):195–214.
[35] Sai Ram KS, Sinha PK. Hygrothermal effects on the bending characteristics of laminated composite plates. ComputStruct 1991;40(4):1009–15.
[36] Sai Ram KS, Sinha PK. Hygrothermal effects on the buckling of laminated composite plates. Compos Struct 1992;21(4):233–47.
[37] Naidu NVS, Sinha PK. Nonlinear finite element analysis of laminated composite shells in hygrothermal environments. Compos Struct 2005; 69:387–95.
[38] Sun CT, Chattopadhyay S. Dynamic response of anisotropic laminated plates under initial stress to impact of a mass. J ApplMech 1975;42(3):693–8.
[39] Sun CT, Chen JK. On the impact of initially stressed composite laminates. J Compos Mater 1985;19:490–504.
[40] Chun LU, Lam KY. Dynamic response of fully-clamped laminated composite plates subjected to low-velocity impact of a mass. Int J Solids Struct 1998; 35(11):963–79.
[41] Sekine H, Hu T, Natsume T, Fukunaga H. Impact response analysis of partially delaminated composite laminates. Trans JSME Ser A 1997;63:131–7.
[42] Hu N, Sekine H, Fukunaga H, Yao ZH. Impact analysis of composite laminates with multiple delaminations. Int J Impact Eng 1999;22:633–48.
[43] Karmakar A, Kishimoto K. Transient dynamic response of delaminated composite rotating shallow shells subjected to impact. Shock Vib 2006;13:619–28.
[44] Jones R. Residual strength of composites with multiple impact damage. Compos Struct 1994;28(4):347–56.
[45] Lam KY, Sathiyamoorthy TS. Response of composite beam under low-velocity impact of multiple masses. Compos Struct 1999;44:205–20.
[46] Chakraborty D. Delamination of laminated fiber reinforced plastic composites under multiple cylindrical impact. J Mater Des 2007;28:1142–53.
[47] Ghosh A. Hygrothermal effects on the initiation and propagation of damage in composite shells. J AircrEngAerospTechnol 2008;80(4):386–99.
[48] Reid A. Larson, Anthony Palazotto, 2006, Low Velocity Impact Analysis of Functionally Graded Circular Plates, ASME 2006 International Mechanical Engineering Congress and Exposition
[49] Shariyat M., Jafari R., 2013, Nonlinear low-velocity impact response analysis of a radially preloaded two-directional-functionally graded circular plate: a refined contact stiffness approach, Composites, Part B: Engineering, 45, 981-994

[50] Shariyat M., Farzan F., 2013, Nonlinear eccentric low-velocity impact analysis of a highly prestressed FGM rectangular plate, using a refined contact law, Archive of Applied Mechanics, 83, 623-641
[51] Khalili S.M.R., Malekzadeh K., Veysi Gorgabad A., 2013, Low velocity transverse impact response of functionally graded plates with temperature dependent properties, Composite Structures, 96, 64-74
[52] Dai H.L., Guo Z.Y., Yang L., 2012, Nonlinear dynamic response of functionally graded materials circular plates subject to low-velocity impact, Journal of Composite Materials, DOI: 10.1177/0021998312458132.